

Integrating AI in NDE: Techniques, Trends, and Further Directions

Eduardo Pérez^{a,b}, Cemil Emre Ardic^{a,b}, Ozan Çakıroğlu^{a,b}, Kevin Jacob^{a,c}, Sayako Kodera^a, Luca Pompa^a, Mohamad Rachid^a, Han Wang^{a,b}, Yiming Zhou^{a,d}, Cyril Zimmer^a, Florian Römer^a and Ahmad Osman^{a,d}

^aFraunhofer-Institut für Zerstörungsfreie Prüfverfahren IZFP, Campus E3 1, 66123 Saarbrücken, Germany

^bTechnische Universität Ilmenau, Ehrenbergstraße 29, 98693 Ilmenau, Germany

^cUniversität des Saarlandes, Campus, 66123 Saarbrücken, Germany

^dHochschule für Technik und Wissenschaft des Saarlandes, Goebenstrasse 40, 66117 Saarbrücken, Germany

ARTICLE INFO

Keywords:

Artificial intelligence
Machine Learning
NDE 4.0
ECT
3MA
UT
TT
VT

ABSTRACT

The digital transformation is fundamentally changing our industries, affecting planning, execution as well as monitoring of production processes in a wide range of application fields. With product line-ups becoming more and more versatile and diverse, the necessary inspection and monitoring sparks significant novel requirements on the corresponding Nondestructive Evaluation (NDE) systems. The establishment of increasingly powerful approaches to incorporate Artificial Intelligence (AI) may provide just the needed innovation to solve some of these challenges.

In this paper we provide a comprehensive survey about the usage of AI methods in NDE in light of the recent innovations towards NDE 4.0. Since we cannot discuss each NDE modality in one paper, we limit our attention to magnetic methods, ultrasound, thermography, as well as optical inspection. In addition to reviewing recent AI developments in each field, we draw common connections by pointing out NDE-related tasks that have a common underlying mathematical problem and categorizing the state of the art according to the corresponding sub-tasks. In so doing, interdisciplinary connections are drawn that provide a more complete overall picture.

1. Introduction

Nondestructive Evaluation (NDE) is one of the key ingredients for ensuring safety, reliability, and efficiency of products as well as infrastructure we use and depend on everyday. In light of challenges such as increasing technological complexity of our industries, aging infrastructure, or the general need to reduce resource consumption, its significance for industry and society is expected to grow dramatically in the near future. Like industry itself, the field of NDE has undergone several transformations, adopting innovations in sensor technology, networking and computing power and more recently, AI methods to cope with the requirements of increasingly complex industries. At the intersection between NDE and Industry 4.0 technologies, the field of "NDE 4.0" has emerged as a confluence of Industry 4.0 digital technologies, physical inspection methods, and business models. It embraces the digital transformation, including digital twins of products and inspection systems, Industrial Internet of Things (IIoT) technologies for seamless networked integration, semantic interoperability through standardized interfaces, common data formats and appropriate meta descriptions, heterogeneous compute power through cloud and edge technologies, and other recent developments. By many, NDE 4.0 is also seen as a potential step to increase automation of current NDE systems, as its growing complexity allows it to handle increasingly sophisticated tasks autonomously.

The present paper provides a survey on the state of the art in the usage of AI methods for NDE, in light of the promises of the NDE 4.0 developments. We discuss to what extent certain levels of automation can now be handled through AI-powered NDE approaches, which advances have been

demonstrated in that regard recently, and which limitations we are still facing. It is illustrative to categorize the degree of NDE automation according to NDE automation levels as suggested in [1], which we later decompose into specific tasks, as well as the common NDE operator levels according to DIN EN ISO 9712 [2]. A level 1 operator is mostly responsible for conducting measurements under the supervision of a higher level personnel and thus, the tasks are easier to automate. On the other hand, the tasks of a level 2 operator (result interpretation and decision making) or even a level 3 operator (modality selection, inspection design and full responsibility of the entire chain) require much higher degree of sophistication.

Since the entire discussion on NDE automation is highly dependent on the considered modality, we treat a selection of NDE modalities in different sections of this paper. As the entire field of NDE is too wide to provide a thorough review in just one paper, we limit our scope to selected, representative modalities: magnetic methods (eddy current testing and micromagnetic methods), Ultrasound, thermography, and at the end also touching on optical inspection techniques.

As a second contribution, the paper attempts to provide connections between the AI-powered NDE tasks and their underlying mathematical problems that are often similar. The common patterns help seeing intersections between related fields that can benefit from interdisciplinary work and give rise to powerful cross-domain AI approaches.

The paper is organized as follows: section 2 reviews magnetic methods, Ultrasound is treated in section 3, in section 4 we discuss thermography, and section 5 we consider optical inspection. The common patterns between AI-powered NDE tasks are elaborated on in section 6 before drawing conclusions in section 7.

Throughout this work, quantities in bold lowercase $\boldsymbol{\nu}$ are vectors, while those in bold uppercase \boldsymbol{M} are matrices. Scalar elements of vectors and matrices are denoted as $\nu(i)$ and $\boldsymbol{M}(i, j)$, respectively. The symbol $(\cdot)^H$ represents the Hermitian or complex conjugate transpose, and $(\cdot)^\dagger$ is the pseudo-inverse. Calligraphic symbols \mathcal{S} denote sets. Further symbols are introduced throughout the work as needed.

2. Magnetic methods

Several NDE methods rely on the magnetic interaction of a probe with the test specimen. These include, amongst others, eddy current testing of electrically conductive materials. During testing, an alternating magnetic field is generated by a coil, which induces eddy currents in the material to be tested. The eddy current density then generates the secondary magnetic field which is measured with a sensor. Typically, the measurement sensor also contains the excitation coil, enabling to infer the eddy current density. The measured parameters are the amplitude and the phase shift to the excitation signal. In the case of ferromagnetic materials, some magnetic properties, which correlate with the mechanical properties of the material, can also be detected with other techniques. For example, the Barkhausen effect, which is caused by the movement of the magnetic domain walls of the sample upon magnetic excitation, can be analyzed. A combination of those two methods together with the analysis of the harmonics of the tangential magnetic field and the incremental permeability [3] is possible, and among such mixed modalities we highlight the Micromagnetic Multiparameter Microstructure and stress Analysis (3MA) II system. The 3MA-X8 system is a further development, focusing on a more robust and less complex device and sensor design [4]. This system also combines eddy current analysis, incremental permeability analysis and harmonic analysis, omitting the Barkhausen noise analysis [4]. These methods find wide application in the field of material characterization as well as defect detection.

2.1. Eddy current testing

Generally, eddy current probe impedance is recorded as a function of probe position and/or excitation frequency, which is used for detecting flaws such as cracks in materials. Inferring those parameters from the impedance measurements is an inverse problem and widely recognized as a complex theoretical problem. Already in 1997 Rekanos et al. [5] suggested the use of Neural Networks (NNs) to tackle the inversion problem. Since then, a number of studies have focused on the detection and evaluation of flaws with the help of Artificial Neural Networks (ANNs). Of particular interest here are defects such as cracks, which could paralyse operations and endanger safety.

Thus, Helifa et al. [6], Harzallah et al. [7], Demachi et al. [8] and Bernieri et al. [9] dealt with the detection and assessment of cracks. While Helifa et al. and Harzallah et al. made use of AI supported inversion for the detection and characterization of surface cracks, Bernieri et al. discussed crack shape reconstruction and compared the results using an ANN and Support Vector Regression (SVR) and Demachi et

Table 1

Crack shape reconstruction results of Bernieri et al. [9]

| | MAE l | MAE a | MAE z_0 |
|-----|---------|---------|-----------|
| SVR | 0.043 | 0.12 | 0.12 |
| ANN | 0.14 | 0.24 | 0.24 |

al. studied the estimation of crack depths in non-magnetic material using a Convolutional Neural Network (CNN) with two convolution layers, two pooling layers and a fully connected layer. They were able to estimate the crack depth within an error of 0.05 mm. For their research, Helifa et al. used a Multilayer Perceptron (MLP) with 21 input neurons corresponding to 21 different sensor positions, a hidden layer with 80 neurons and hyperbolic tangent activation function and an output layer with a linear activation function. The network was trained on simulated data and achieved relative errors of 2.5 % for the depth and 2 % for the length of the cracks. Harzallah et al. took a similar approach and used a MLP with 1 input layer, 1 hidden layer and 1 output layer and trained it on simulated signals. They stopped the training after 30 epochs at an Mean Squared Error (MSE) of about $5 \times 10^{-7} \text{ mm}^2$ for the train and validation data, while the test error was about $1 \times 10^{-2} \text{ mm}^2$ for length and depth of the crack. On the other hand, Bernieri et al. discussed crack shape reconstruction and compared the results using an ANN and SVR. The database for the training was constructed by simulation. A $200 \text{ mm} \times 200 \text{ mm} \times 2 \text{ mm}$ aluminum plate was simulated, where the defect region was divided into a regular grid of 20×4 elements, imposing defect depth z_0 and height a steps of 0.5 mm and length l step of 1 mm. This way, a data set of 200 simulated magnetic field maps was obtained. They found that the SVR outperformed the three layered MLP in terms of Mean Absolute Error (MAE) as shown in table 1.

If we move into the area of nuclear reactors, not only cracks but even minor flaws are of great interest and must be reliably recognised for safe operation. Thus, Song et al. [10] as well as Yusa et al. [11] have dealt with the investigation of flaws in steam reactor pipes. In order to train a NN on an synthetic dataset generated by simulation to determine the type and size parameters of flaws in steam generator tubes, Song et al. [10] built a synthetic database with 400 ECT signals generated from 200 axisymmetric machined grooves in four types with two test frequencies per flaw. They used a probabilistic NN for the flaw classification and a back propagation network for the flaw sizing. This resulted in an overall accuracy of 91 % in the determination of the flaw type while the correlation coefficients between actual and estimated size parameters exceeded 0.97. For the reconstruction of natural cracks that occurred in steam generator tubes, Yusa et al. [11] modeled cracks as a pixel map and simulated eddy current signals from that. NNs were trained using a database that contained 400 cases of simulated data. Subsequently, genuine natural cracks that were found in a steam generator tube of a nuclear power plant were measured and reconstructed using the trained

network, demonstrating good agreement with the results of the destructive inspection carried out afterwards. Wrzuszczak [12] detected flaws in conducting layers of aluminum and copper as well as in ferrous tubes by using NNs. They tried MLPs and Radial Basis Function (RBF) networks and showed, that the RBF outperformed the MLP on this task, resulting in a lower training time.

Many other Eddy Current Testing (ECT) tasks also can be improved by the aid of AI methods. For instance, Glorieux et al. [13] studied the electrical conductivity profiles using NN inversion of multi-frequency eddy current data. A MLP consisting of three sigmoid input neurons and one linear output neuron was trained on 2000 simulated conductivity profiles which was obtained using piecewise constant functions (20 segments). Afterwards the network was tested on real data in form of artificially stacked samples and showed good results. On the other hand, Rao et al. [14] used NNs to test austenitic stainless steel welds in order to detect and characterize longitudinal and transverse surface-breaking notches. On the basis of multi-frequency eddy current data they evaluated the depth of the surface-breaking notches in the welds with a maximum deviation of 0.08 mm. Kuzmin et al. [15] applied NNs for recognizing rail structural elements in magnetic and eddy current defectograms. They investigated three classes of structural elements of a railroad track: (1) a bolted joint with a straight or beveled rail connection, (2) a flash butt rail weld, and (3) an aluminothermic rail weld. Patterns that couldn't be assigned to these three classes were considered as defects and attributed to a separate fourth class. The used NN contained 780 input neurons, a hidden layer with 800 neurons and four output neurons. The training set contained 16287 real and 8323 generated samples of structural elements of three classes and 11417 real samples of conditional defects. The validation set contained 4098 generated samples of structural elements of three classes and 1903 real samples of conditional defects, whereas the test set consisted of 4098 and 1902 samples of the same kinds, respectively. The achieved accuracy was 99.83 % on training data, 99.45 % on validation data and 99.23 % on test data. In order to identify broken wires within a wire rope, Cao et al. [16] used a RBF network (3 input neurons, 2 output neurons, one hidden layer) and were able to not only detect if there was a broken wire, but also estimate how many wires were broken. Further Ali et al. [17] gave a review on system development in ECT and technique for defect classification and characterization as well as an overview of AI methods used in defect measuring, while AbdAlla et al. [18] gave a review of challenges in improving the performance of ECT as well as of AI methods used in defect measuring.

2.2. Barkhausen effect

The Barkhausen effect was discovered in 1919 by the German physicist Heinrich Barkhausen. Barkhausen noise consists of discontinuous changes in the magnetization of ferromagnetic materials in a changing external magnetic field. This is explained by the fact that the shifting Bloch walls are temporarily "trapped" by the lattice perturbations

and only break free from their anchoring abruptly when the driving force is increased (Barkhausen event). A further increase of the field strength causes the magnetization in the domains to rotate in the direction of the external magnetic field. When applying an external alternating magnetic field to a ferromagnetic specimen, the resulting Barkhausen noise can be recorded with a Hall probe. Since the Barkhausen events are tightly connected to the lattice defects in the material, the characteristics of the recorded Barkhausen noise correlate with the mechanical properties of the material, which are also linked to lattice defects.

Consequently this enables the evaluation of magnetic properties of the material under investigation, like done by Maciusowicz et al. [19], but also the mechanical properties of the material, like Wang et al. [20] and Zhang et al. [21] show. Consequently, this enables the evaluation of magnetic properties of the material under investigation as well as the mechanical properties of the material. Aiming to identify the magnetic properties of the test materials, Maciusowicz et al. [19] evaluated the grade and the magnetic directions of conventional and high grain oriented electrical sheets subjected to selected surface engineering methods. Several Machine Learning (ML) techniques (decision trees, discriminant analysis, Support Vector Machine (SVM), naïve Bayes, k -Nearest Neighbour (k NN), ensemble classifiers and ANN) are compared. The achieved results generally indicated an approximately 10 % advantage of the deep learning model over the classical ones in terms of accuracy in each of the considered cases. For determining the mechanical properties of the test objects, Wang et al. applied a NN for the steel stress detection based on Barkhausen noise in order to achieve robust results against temperature fluctuations, which have an impact on the stress as well as on the received signal. Zhang et al. predicted yield strength, ultimate tensile strength and elongation of cold rolled strips by the use of a fully connected NN with two hidden layers (five input nodes, three output nodes, five nodes in first hidden layer and six nodes in second hidden layer). In the test results the largest relative errors of yield strength, tensile strength and elongation are 5.66 %, 2.99 % and 3.62 %, respectively.

2.3. 3MA II and further combinations of methods

By combining several methods into one framework, the robustness, reliability and precision with regard to the determination of mechanical properties can be increased. An example of such a combination of methods is given by the 3MA II device, which not only combines eddy current and Barkhausen noise measurements, but further also measures the harmonic distortion of a pure sinusoidal excitation as well as the incremental permeability of the material. Thus 3MA or similar devices are limited to ferromagnetic materials, but can be used in a wide range of applications, including but not limited to the estimation of mechanical properties, as Jedamski et al. [22], Wang et al. [23], Xing et al. [24] as well as Sheng et al. [25] have done in their work, whereby Sheng et al. further combined the 3MA II with Electro Magnetic Acoustic Transducer (EMAT).

Table 2

Results of the estimation of hardness and carburization depth from Jedamski et al. [22], comparing the linear regression and the neural network approach

| | | RMSE Hardness (HV1) | RMSE Carburiza- tion Depth (mm) |
|-------------------|-------------------|---------------------------|--|
| Training score | linear regression | 12.5 | 0.074 |
| | neural network | 7.1 | 0.03 |
| Test score | linear regression | 17.9 | 0.13 |
| | neural network | 16.4 | 0.103 |

In their work, Jedamski et al. [22] determined the hardness and the case hardening depth using linear regression as well as NNs and compared the results. Their sample set consists of 54 discs made from one batch of steel AISI 4820 (DIN 18CrNiMo7-6) with a diameter of 68 mm and a thickness of 20 mm. The samples were gas carburized and oil quenched in 27 variations. The best results achieved are shown in table 2.

Both Wang et al. [23] and Xing et al. [24], predicted the surface hardness in ferromagnetic Materials by using a device quite similar to 3MA II. Wang et al. [23] studied the prediction of surface hardness in carbon steels, referred as Cr12MoV steel, 45 steel, and martensitic stainless steel of 3Cr13 in Chinese standards. For each material, a total of 27 specimens (200 mm × 60 mm × 3 mm) were cut from a steel plate along its rolling direction. Afterwards, quenching, followed by tempering, was performed. The NN used to predict the surface hardness consisted of 31 input neurons for selected magnetic measurands, one hidden layer with 50 neurons and one output neuron. The achieved Root Mean Squared Error (RMSE) of the predictions of surface hardness was 7.52 HV30 for the Cr12MoV steel, 4.27 HV30 for the 3Cr13 steel and 7.44 HV30 for the 45 steel. Xing et al. [24] on the other hand, evaluated the surface hardness only on Cr12MoV steel. For that purpose, a batch of 8 plates with dimensions of 250 mm x 60 mm x 3 mm were cut from the cold work die steel plates and were quenched. Afterwards, hardness (HV30) was tested on 3 positions per plate. A simple feed forward network with an input layer for the micromagnetic measurands, two hidden layers with 10 nodes and an output layer with one node for the hardness was used. The MAE and Standard Deviation (SD) in surface hardness prediction were approximately 1.02 HV and 1.04 HV, respectively.

In order to predict the Tensile Strength (R_m) and surface hardness (HA) in pipeline steel, Sheng et al. [25] further combined 3MA II with EMAT. Training and validation data were acquired on seventeen pipeline steel samples (300 mm × 750 mm, thickness > 12 mm) of various lots and grades. For the test data an X65 pipeline steel plate with a size of 4 m × 12 m with a tensile strength of 670 MPa was prepared. The tensile strength was assumed to be constant over the whole plate, hardness was tested at 65 points distributed over the plate. The prediction results show that, compared to MLP,

Table 3

Comparison of the results from different approaches to estimate tensile strength and hardness from Sheng et al. [25]

| | R_m SD (MPa) | HA RMSE (HV1) |
|---------|-------------------|------------------|
| XGBoost | 17.69 | 11.85 |
| MLP | 31.9 | 25.45 |
| RF | 19.47 | 15.49 |
| DNN | 18.47 | 14.22 |

Table 4

Comparison of the results from different approaches to estimate the DBTT from Grönroos et al. [26]

| | | | HLR | SVR | ANN |
|------------------------------------|-----------|-------|-------|-------|-----|
| 10-fold cross- validation score | MAE (°C) | 13.67 | 13.58 | 12.7 | |
| | MAE (°C) | 9.32 | 8.68 | 9.21 | |
| Training score | RMSE (°C) | 14.49 | 13.63 | 12.57 | |
| | R^2 | 0.97 | 0.97 | 0.98 | |
| Test score | MAE (°C) | 17.1 | 17.77 | 16.04 | |
| | RMSE (°C) | 18.67 | 20.4 | 22.08 | |
| | R^2 | 0.95 | 0.94 | 0.93 | |

Random Forest (RF), and Deep Neural Network (DNN), the approach based on the extreme Gradient Boosting (XGBoost) was found to yield the highest prediction accuracy in terms of RMSE and SD for the test data set, as shown in table 3.

Another example of AI aided estimation of mechanical properties based on the combination of several techniques is given by Grönroos et al. [26], who estimated the embrittlement of a nuclear reactor pressure vessel, which is measured as the Ductile-Brittle Transition Temperature (DBTT). For that purpose, they combined 3MA II with Micromagnetic Inductive Response and Barkhausen Emission Method, Magnetic Adaptive Testing, Direct Current Reversal Potential Drop, Thermoelectric Power Measuring Method and Ultrasonic Testing (UT) to collect data on standard Charpy V-notch samples made out of six different steel alloys that had been treated in different irradiation conditions. Their data set consists of 29 nondestructively measured parameters and ductile-brittle transition temperature data for 157 samples. Several machine learning methods were compared: linear Huber Loss Regression (HLR), SVR and an ANN consisting of 19 input neurons, one output neuron, 2 hidden layers with 16 and 8 neurons respectively and two dropout layers in between. The results in terms of RMSE, MAE and Coefficient of Determination (R^2) are shown in table 4.

2.4. 3MA-X8

In comparison to the 3MA II, omitting the Hall sensor, as well as the Barkhausen noise and eddy current coils simplified the probe to a voltage-controlled electromagnet [4]. By exciting the electromagnet with a low- and high

Table 5

Classifiability and quantifiability comparison of the 3MA-X8 feature spaces on tensile test data [29]

| Feature space | LDA & k NN accuracy (%) | | MLR | |
|----------------|------------------------------|------------------------------|--------------------|--------------|
| | Random k FCV | Class based validation | RMSE (% R_e) | R^2 (%) |
| 21-dimensional | 64.05 | 63.08 | 4 | 93.6 |
| Extended | 95.14 | 94.21 | 1.96 | 98.46 |

frequency component and measuring the voltage and current of the probe, features of the three methods of measurement, eddy current analysis, incremental permeability analysis and harmonic analysis, are extracted [4]. This simplification leads to a more robust system better suited for higher measurement speeds and sensor arrays [4]. The implementation of ML-Methods considerably enhanced precision and robustness of the 3MA-X8 system even further. New approaches improved the application fields of process optimization in steel mills and reactor safety research in particular [27, 28].

Youssef et al. [29] describes initial studies on improving the accuracy by extending the feature space. In the feature space extension, the available time signals are analyzed in more detail by using Fourier transform, a qualitative hysteresis reconstruction and a multidimensional curve tracing approach, where mathematical characteristics such as high points, zero points and axis intercepts are included as features. The underlying data was acquired in a tensile test on three different normalized materials, 100Cr6, C45 and S235 where each material was stressed in increments of 5 % up to 50 % of its Yield Strength (R_e). To classify the stress levels independently of the material, a Linear Discriminant Analysis (LDA) reduces the feature space down to two dimensions before a k NN-Classifer with $k = 10$ predicts the class. Regarding the classifiability a k -Fold Cross Validation (k FCV) with a randomized train-test-split and a $k = 10$ was used to determine the accuracy before and after feature space extension. Considering the quantifiability of the stress levels, a class based validation assigns every second stress level to the test data set. Both, the classifiability and the quantifiability were improved significantly, as shown in table 5 below using the accuracy. To further describe the quantifiability, a Multiple Linear Regression (MLR) predicts the stress level also based on a class based validation assigns every second stress level to the test data set. The quantifiability was also improved significantly, as shown in table 5.

Youssef et al. [30] further investigates different ML methods based on the same experimental setup as in the previous study [29], while also comparing the performances of the feature spaces. Specifically, it was compared whether and with what effort the prediction quality of MLR can be achieved under similar conditions with SVR and MLP-Regression with a single hidden layer and linear activation functions, which are frequently used in regression problems. Under variation of

Table 6

Different ML methods of the 3MA-X8 feature space on tensile test data [30]

| Model | Feature space | | RMSE | R^2 |
|--------------------|----------------|-------|------------|-------|
| | | | (% R_e) | (%) |
| MLR | 21-dimensional | Train | 7.99 | 78.07 |
| | | Test | 7.83 | 69.35 |
| MLR | Extended | Train | 2.3 | 98.19 |
| | | Test | 4.99 | 87.54 |
| SVR | 21-dimensional | Train | 8.32 | 69.85 |
| | | Test | 7.62 | 66.69 |
| SVR | Extended | Train | 4.11 | 93.96 |
| | | Test | 4.49 | 90.33 |
| MLP- Regression | 21-dimensional | Train | 10.33 | 63.42 |
| | | Test | 9.48 | 55.08 |
| MLP- Regression | Extended | Train | 5.54 | 89.49 |
| | | Test | 5.69 | 83.82 |

the regularization parameter c in the SVR and variation of the number of neurons in the hidden layer of MLP-Regression, the best performing model was chosen. The train data RMSE and R^2 of these models are shown in table 6. The extended feature space has performed significantly better overall. However, neither the SVR nor the MLP-Regression produced significant improvements under the conditions explained.

Youssef et al. [27] further published the application of ML methods with the 3MA-X8 in process optimization in steel mills, proving the successful application of the prior investigated methodologies [30, 29] in an industrially relevant environment. The focus was on the detection of local hardness inhomogeneities in heavy plates for the pipeline industry, where the task was to detect hardness differences of ± 30 HV 10 at a minimum diameter of 10 mm. Supervised ML methods sufficiently suppressed various interferences coming from residual fields and scale layers. Unsupervised ML algorithms suppressed the lift-off influence based on a series of measurements with a sensor lift-off variation of 0 mm to 3 mm on sample heavy plate segments. Based on these findings, the product "PLAMAT-MM-32M" was developed for the use in steel mills.

Zimmer et al. [28] described the application on Reactor Pressure Vessel (RPV)-steel, where the objective is to differentiate between stress and microstructural influences. The materials used are 20MnMoNi5-5 and 22NiMoCr3-7 with further variation levels introduced by Low-cycle fatigue (LCF) tests and tensile tests which leads to a more complex dataset in comparison to prior studies [30, 29]. Regarding the features of the dataset, the extended feature space was further extended by the raw signal samples as features themselves. To illustrate the ambiguities between microstructure and stress influences, fig. 1 shows a single feature of the 21-dimensional feature space. For stress-independent microstructure characterization, a train-test-split randomly divided the dataset into 80 % train data and 20 % test data. Based on this dataset, an LDA performed a dimensional reduction to four dimensions. The first two

Table 7

Hierarchical modeling of the 3MA-X8 feature space on RPV-steel data [28]

| Feature Space | Subgroup | Train RMSE (MPa) | Test RMSE (MPa) |
|----------------|---------------|------------------|-----------------|
| 21-dimensional | Global | 43.91 | 40.10 |
| Extended | Global | 13.98 | 14.66 |
| Extended | Tensile tests | 9.94 | 11.01 |
| Extended | LCF tests | 9.36 | 10.87 |
| Extended | 20MnMoNi5-5 | 8.14 | 8.93 |
| Extended | 22NiMoCr3-7 | 10.91 | 13.95 |

dimensions shown in fig. 2 indicate a much clearer separation of individual material variants illustrated by the the point clouds. Subsequently, a k NN-Classifer with $k = 5$ neighbors and uniform weighting was trained. The extended feature space significantly improves the model with 0.77 % misclassified data points of the test data compared to 3.89 % of the 21-dimensional feature space. For microstructure-independent stress determination, a MLR predicted the stress in MPa. For the train-test split, the dataset was divided into seven segments along the target variable, alternating between train and test data to detect overfitting and overgeneralization. A hierarchical approach was performed, dividing the dataset in different subgroups prior to fitting the MLR. This approach was able to improve the models accuracy significantly in comparison to the global models as shown in table 7.

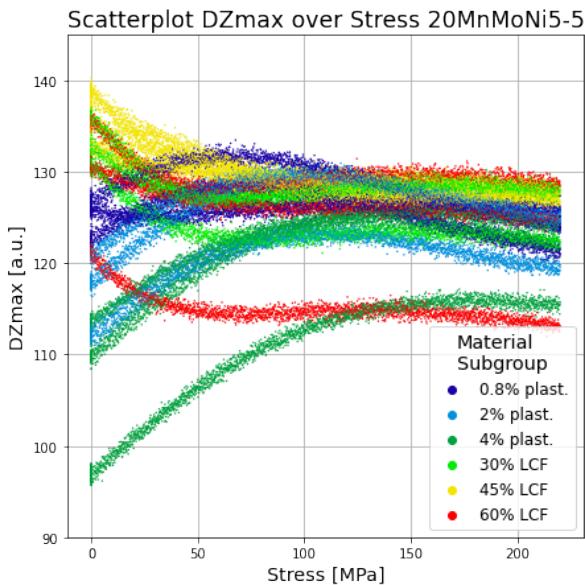


Figure 1: 20MnMoNi5-5 stress-dependent scatterplot of feature DZmax (maximum value of incremental permeability) which is not sufficient to differentiate the material variants considered in [28]

Youssef et al. [4] systematically examined the previous approaches and combined them into a global methodology. In

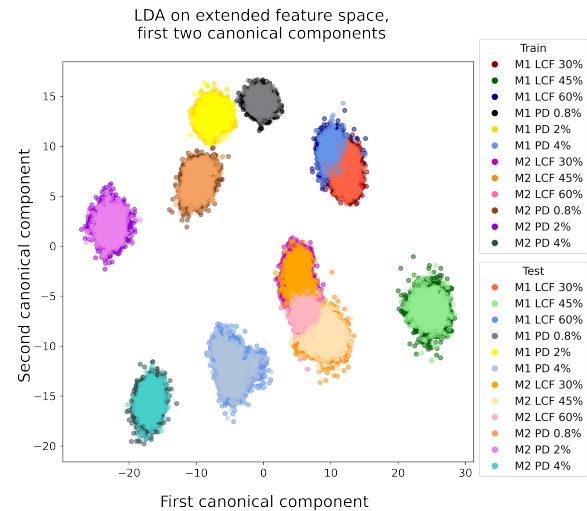


Figure 2: First two canonical components transformed by LDA of the extended feature space [28], demonstrating a clearer separation of individual material variants compared to fig. 1. "M1" refers to the material 20MnMoNi5-5 and "M2" refers to the material 22NiMoCr3-7

Table 8

Iterative polynomial extension of the 3MA-X8 feature space [4]

| Feature Space | Polynomial Grade | | RMSE (% R_e) | R^2 (%) |
|----------------|------------------|-------|-----------------|-----------|
| 21-dimensional | 1 | Train | 6.721 | 81.0 |
| | | Test | 6.567 | 78.2 |
| 21-dimensional | 11 | Train | 3.014 | 96.2 |
| | | Test | 2.863 | 95.9 |
| Extended | 4 | Train | 0.830 | 99.7 |
| | | Test | 0.974 | 99.5 |

order to map nonlinear relationships between the feature space and the target variable, a polynomial extension linearizes the feature space iteratively, until the model quality reaches an optimum. This systematic approach was applied on the RPV-steel materials and experimental setup of the prior paper [28]. To determine the stress in % R_e , a MLR was conducted. Regarding the train-test split, a segment based approach was used, dividing the dataset into segments along the target variable alternating between train and test data. Before the main model was trained, the number of segments was determined by iteratively increasing the number of segments, until no significant improvement in the MLR occurs. As a result, the train-test split divided the data into 21 train segments and 20 test segments. To show the improvement of the iterative polynomial extension, different iterations and feature spaces were examined as shown in table 8. Comparing the eleventh polynomial grade of the 21-dimensional feature space to the fourth polynomial grade of the extended feature space it is clear, that in this example the use of the extended feature space yields a significantly better result with fewer iterations.

3. Ultrasound

Ultrasound signals, characterized by frequencies from 20 kHz to the gigahertz range and beyond human hearing, are pivotal in computational imaging, especially in NDE. A key technique in this domain is pulse-echo imaging, which involves the capture and utilization of scattered echoes arising from inhomogeneities within the measurement area.

In its simplest form, ultrasound data can be modeled via the wave equation [31], so that the measured pressure field p obeys

$$\nabla^2 p - \frac{1}{c^2} \frac{\partial^2 p}{\partial t^2} = -s. \quad (1)$$

In (1), $p = p(t, \mathbf{x})$ is a pressure field that depends on the time t and position $\mathbf{x} \in \mathbb{R}^d$ for a d -dimensional space. The speed of sound $c = c(\mathbf{x})$ may in general vary over space due to changes in density and compressibility, and the term $s = s(t, \mathbf{x})$ represents sources in the medium. Alternatively, when working with a monochromatic field or after separation of variables, the frequency domain representation of the field obeys the Helmholtz equation, meaning

$$\nabla^2 \tilde{p} + k^2 \tilde{p} = -\tilde{s}, \quad (2)$$

where quantities with a tilde ($\tilde{\cdot}$) are frequency domain counterparts to the corresponding quantities without the hat. As a result, $\tilde{p} = \tilde{p}(\omega, \mathbf{x})$ and $\tilde{s} = \tilde{s}(\omega, \mathbf{x})$ depend on the angular frequency ω , and all quantities including the wavenumber $k = k(\omega, \mathbf{x})$ can vary over space.

A common practice is to obtain approximate solutions to eqs. (1) and (2) by discretizing them into systems of linear equations. In the time domain, the problem can be formulated as

$$\mathbf{p} = \mathbf{G}\boldsymbol{\gamma}, \quad (3)$$

where \mathbf{p} is obtained by discretizing p , e.g. along the temporal and spatial axes. The matrix \mathbf{G} is referred to as the *model* or *measurement* matrix, and its formulation depends on the task. Similarly, the vector $\boldsymbol{\gamma}$ encodes the sought-after parameters, and its exact definition depends on the application.

Many ultrasound-based NDE techniques revolve around estimating the speed of sound c , the wavenumber k , or the underlying physical parameters that determine them. Quantitative and qualitative estimates of these parameters are employed in detection, localization, imaging, classification, and more. Additionally, the amount of information about these parameters depends on the way in which the data is measured. As a result, the optimization of measurement parameters is another well-researched task. We discuss recent trends and open opportunities in the application of artificial intelligence to ultrasound NDE tasks next.

3.1. Ultrasound Imaging

Conventional techniques like Plane Wave Imaging (PWI) and Full Matrix Capture (FMC) transmit several incident waves from different angles and/or locations and collect the

scattered echoes with one or more receivers [32]. These traditional techniques mostly depend on augmenting the number of transmitted signals to enhance the accuracy and resolution of the reconstruction or classification.

A mathematical model for the received signal in the ultrasound imaging can be defined in the form of matrix-vector multiplication as

$$\tilde{\mathbf{p}}_{\text{rec}} = \mathbf{G}\boldsymbol{\gamma} + \tilde{\boldsymbol{\eta}}. \quad (4)$$

where $\tilde{\mathbf{p}}_{\text{rec}}$ is the received or measured frequency domain signal vector carrying distinct samples, $\boldsymbol{\gamma}$ is the parameter of interest, and $\tilde{\boldsymbol{\eta}}$ represents complex additive noise. A common choice for the construction of \mathbf{G} is to employ the first-order Born approximation and Green's function for a homogeneous, isotropic medium, as shown in [33]. Following this model, the inverse scattering problem in which $\boldsymbol{\gamma}$ is estimated from the measurement data $\tilde{\mathbf{p}}_{\text{rec}}$ can be reformulated as an optimization problem of the form

$$\hat{\boldsymbol{\gamma}} = \underset{\boldsymbol{\gamma}}{\operatorname{argmin}} \lambda R(\boldsymbol{\gamma}) + \|\tilde{\mathbf{p}}_{\text{rec}} - \mathbf{G}\boldsymbol{\gamma}\|_2^2, \quad (5)$$

where $R(\cdot)$ is a regularizer and λ regulates its impact on the solution.

One example for the solution of eq. (5) is the case where $\tilde{\mathbf{p}}_{\text{rec}}$ is represented sparsely by \mathbf{G} . In that case, $R(\cdot) = \|\cdot\|_1$ and $\boldsymbol{\gamma}$ can be estimated by harnessing a reduced amount of measurement data without reducing performance; in some cases, even by exploiting just a single acquisition from each element of the ultrasound transducer array with optimal excitation [33, 34, 35, 36]. There are several conventional sparse data recovery algorithms, i.e. the Iterative Shrinkage-Thresholding Algorithm (ISTA) [37] based on proximal gradient descent, its accelerated version Fast ISTA (FISTA) [38] and the Alternating Direction Method of Multipliers (ADMM) [39] which splits the problem into simpler subproblems which separately focus on addressing the reconstruction fidelity and promoting sparsity through a penalty function. However, all of these algorithms work iteratively and come with a significant computational cost and time expense. Hence, novel methodologies based on neural networks have emerged that lower the reconstruction time without compromising the reconstruction accuracy.

In the next sections, we explore different artificial intelligence approaches to the inverse problems involved in imaging. One approach focuses on designing conventional neural network architectures to tackle the inverse problem, while the other involves reconstruction based on the model of the data and well-known classical optimization algorithms.

3.1.1. Ultrasound Imaging with Conventional Deep Learning Architectures

A self-supervised auto-encoder network that minimizes the MSE between \mathbf{p}_{rec} and $\hat{\mathbf{p}}_{\text{rec}}$ is employed in [40]. This network processes the projection of measurement data in the image domain, i.e. the intermediate quantity $\tilde{\boldsymbol{\gamma}} = \mathbf{G}^H \mathbf{p}_{\text{rec}}$ which resembles Synthetic Aperture Focusing Technique (SAFT). After the autoencoder network yields the reconstruction $\hat{\boldsymbol{\gamma}}$ as

training output, its projection to the measurement domain is calculated this time as $\hat{p}_{\text{rec}} = G\hat{\gamma}$. The results show that the autoencoder gives a similar Contrast-to-Noise Ratio (CNR) and the same axial Full-Width at Half Maximum (FWHM) as conventional Delay and Sum (DAS) beamforming using 75 Plane Waves (PWs), as well as a lower FWHM in lateral direction, in spite of exploiting only one PW. Similarly, based on Deep Residual Learning (DRL) [41], a method for removing the vanishing gradient problems in the neural networks is proposed in [42]. Firstly, the measured signal is linearly mapped to the image domain using a fully connected network as $\bar{\gamma} = W p_{\text{rec}}$ and the elements of the matrix W are learned using the conventional Stochastic Gradient Descent (SGD) training algorithm. After obtaining the initial estimation of the reconstruction data, a second algorithm employing DRL is used to obtain $\hat{\gamma}$ from the initial estimate $\bar{\gamma}$. The authors perform a comparison of Peak Signal-to-Noise Ratio (PSNR) with another residual sparse data reconstruction network called ReconNet [43]. The algorithm demonstrates improved PSNR and faster reconstruction than ReconNet.

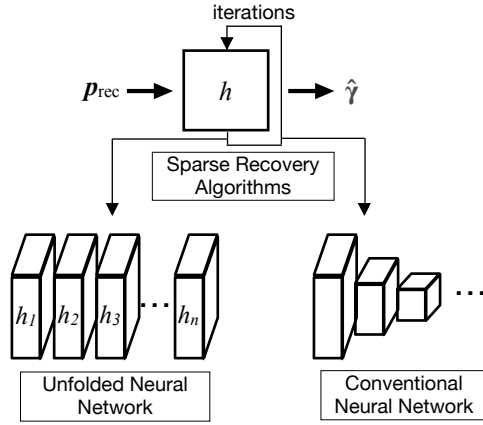


Figure 3: Inversion through unfolding of classical algorithms (left) or direct replacement via neural networks (right)

Artifact removal by means of Generative Adversarial Neural Networks (GANs) is studied in [44]. GANs consist of two different network structures: one generates data and the other discriminates whether the data belongs to the labeled data or was transferred from the generator network. This process continues until the discriminator network fails to differentiate between the two groups. In [44], the input data fed to the generator network is obtained as $\bar{\gamma} = G^\dagger p_{\text{rec}}$ where \dagger represents the pseudo-inverse. A DRL [41] architecture is employed as a generator network, while the discriminator uses a CNN architecture to classify between two groups of images. Additionally, between the generator and discriminator networks, another block is located which tunes the output of the generator network in order to generate a feasible set of images instead of overemphasizing the noise values of the pixels.

3.1.2. Ultrasonic Imaging with Model-Based Deep Learning

In ultrasound signal processing, integrating prior knowledge, such as structure and physics, is crucial [45]. Model-based algorithms with domain knowledge, such as message-passing techniques in ultrasound imaging [46], offer interpretability but depend on specific expertise. Conversely, data-driven methods, particularly Deep Learning (DL), adapt to diverse scenarios without domain-specific knowledge [47, 48], but require extensive data and lack explainability due to their opaque nature. Recently, *model-based deep learning* has been proposed to combine the advantages of both approaches [49].

Model-based deep learning, which merges prior models with DNNs, builds on ideas from over a decade ago. An early example, the Learned ISTA (LISTA), incorporated neural network layers into ISTA for sparse signal recovery [50]. A recent survey by Shlezinger explores this field, outlining concepts, design strategies, and applications. The survey categorizes model-based deep learning into two main types: *model-aided networks*, which integrate complete DNNs with standard model-based algorithms, such as *deep unfolding* or *algorithm unrolling* [51]; and *DNN-aided inference*, which replaces parts of the original approach with DNNs. As an example of DNN-aided inference, [52] leverages generative models to map a lower-dimensional vector to an approximation of the sparse vector γ , aiding subsequent optimization processes.

The integration of model-based deep learning into beamforming represents a significant development in ultrasound imaging. Sloun advanced this field by integrating deep learning methods into various aspects of ultrasound imaging, including scanning modes and digital receive beamforming techniques [53]. Concurrently, Luijten explored the combination of traditional ultrasound signal processing with model-based deep learning, transforming beamforming into parameter estimation problems [54]. A model-based DNN based on Minimum Variance (MV) beamforming was developed, achieving high-quality image reconstruction with reduced computational demands [55, 56]. The resulting neural network architecture, dubbed Adaptive Beamforming by Deep LEarning (ABLE), was shown to outperform DAS and compete with MV beamforming with regards to CNR, FWHM, and MAE at a lower computational cost.

Deep unfolding, recognized for its transparency, reliability, and simplicity, is a prominent method in model-based deep learning, as highlighted in [57]. Originating from the Aperture Domain Model Image REconstruction (ADMIRE), this technique has proven effective in improving image quality and suppressing acoustic clutter, as demonstrated in studies by Khan [58]. In the context of Contrast-Enhanced Ultrasound (CEUS), the novel model-based DNN named Convolutional Robust Principal Component Analysis (CORONA) has been introduced [59]. CORONA unfolds an iterative algorithm into a fixed-length architecture, enhancing convergence and image quality.

Moreover, Compressed Sensing (CS) with model-based deep learning has significantly advanced optimal subsampling

pattern exploration. By assuming a finite rate of innovation (FRI) structure in beamformed signals from frequency-domain beamforming [60] or compressed beamforming by Convolutional Beamforming Algorithms (COBA) [61], an efficient model-based DNN utilizing a modified LISTA has been developed. This approach, as shown in [62], considerably reduces array elements, sampling rates, and computational times while preserving imaging quality. Furthermore, Huijben applied the Gumbel-Softmax reparameterization trick with LISTA, introducing the Deep Probabilistic Subsampling (DPS) approach [63] which turns the combinatorial problem of choosing k out of n samples optimally into one that can be solved with gradient-based methods. In contrast, traditional approaches such as the ones explored in [64] rely on greedy methods and search for suboptimal solutions in order to remain tractable in large scenarios.

Within the DPS framework, an optimal spatial subsampling design for single-channel synthetic aperture imaging has been developed, focusing on maximizing Fisher information [65] or minimizing reconstruction error [66]. In multichannel imaging, the design of subsampling matrices based on information theory-based and task-based targets was studied within the DPS framework [67]. Additionally, Joint DPS (J-DPS) has been introduced in [68] for the structured selection of transmitters, receivers, and Fourier coefficients during measurements. The parallel network architecture, illustrated in Figure 4, significantly reduces trainable parameters, enhancing the practicality of the CS pattern in hardware applications.

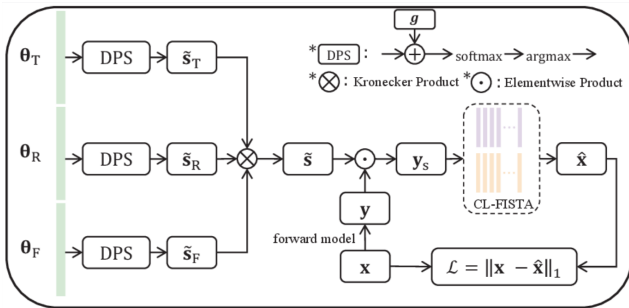


Figure 4: Structure of Joint DPS Algorithm

3.2. Computed Tomography and Full Waveform Inversion

In Ultrasound Computed Tomography (UCT), internal cross-sections of an object are derived from ultrasound propagation models and measurements collected from sensors on the object's surface [69]. The cross-sections are quantitative in nature, accurately describing the physical parameters of the object under test. Traditional UCT methods use the first-order Born approximation [70] and linear ray models, yielding algorithms akin to X-ray imaging. For instance, Algebraic Reconstruction Technique (ART), typical in X-ray, is applied for slowness maps in masonry pillars, aiding in computing Young's modulus [71]. Similarly, [72] employs Simultaneous Iterative Reconstruction Technique (SIRT) for slowness map generation. Nonetheless, these approaches overlook critical

phenomena like refraction and multiple scattering, thereby constraining resolution and quantitative interpretability [73].

The ultrasound community has recently adopted techniques from geophysics and seismology, notably Full Waveform Inversion (FWI). This method emphasizes the accurate solution of eqs. (1) and (2) to simulate realistic wave propagation [74]. It is typically framed as the nonlinear least squares problem

$$\underset{\gamma}{\operatorname{argmin}} \|G(\gamma) - p_{\text{rec}}\|_2^2, \quad (6)$$

where G represents a nonlinear function mapping parameters γ to simulated data, typically via a differential equation solver. Alternatively, the problem can be reformulated in the frequency domain using \tilde{p}_{rec} .

FWI has shown promise in medical ultrasound, particularly in high-resolution brain imaging [75]. Yet, its implementation is demanding, requiring significant computational resources for precise ultrasound simulation. Moreover, the ill-posed nature of the problem in eq. (6) necessitates effective regularization.

Neural networks are increasingly utilized in tomography with and without FWI, either as a component substitute or a complete replacement for traditional methods. For instance, in [76], neural networks aid in detecting inclusions within reactor tanks. Here, γ denotes the presence of inclusions. A preprocessing step transforms the measurement data p_{rec} into a time-of-arrival vector τ which is then mapped by a classification CNN Ψ to an estimated $\hat{\gamma}$. Similarly, [77] employs a neural network for inversion in material parameter estimation. They use a modified Galerkin method for simulation and a CNN for inversion, focusing on a task-based approach with a cost function that minimizes the difference between predicted and reference material parameters γ . These studies, along with others reviewed in [1], highlight the growing role of CNNs in ultrasonic computed tomography (UCT) and non-destructive testing (NDE).

UCT is more common in medical imaging than in NDE, yet it remains nascent in medical applications. Nevertheless, progress in integrating UCT with artificial intelligence is more pronounced in medical imaging. A prime example is [78], where authors reconstruct a speed of sound map γ using a small number of sensors. Differing from previous studies, they apply a network in the image domain: a low-resolution image $\tilde{\gamma}$ obtained using a bent ray model is refined using a U-Net [79], trained to match high-resolution maps obtained with extensive sensor data. The training focuses on optimizing the reconstruction fidelity $\|\Psi(\tilde{\gamma}) - \gamma\|_2^2$. Similar approaches are seen in NDE, such as in [80], where a CNN computes γ from limited plane wave data and forward modeling is done with Matlab's k-wave toolbox. The rising use of CNNs in medical imaging underscores their significance in advancing UCT applications.

A separate approach to modeling and inversion is provided by Physics-Informed Neural Networks (PINNs) [81, 82, 83]. PINNs break away from the previous patterns of using classical

Table 9
Classification of ML-aided UCT and FWI approaches

| Approach | Forward method | Inverse method |
|----------|----------------|----------------------|
| Direct | classical | CNN |
| Two-step | classical | preprocessing CNN |
| PINN | DN | DN |

methods of forward modeling. Instead, the focus is shifted onto the representation of solutions to the governing differential equations. To this end, a neural network $u_\theta : (\omega, \mathbf{x}) \mapsto p(\omega, \mathbf{x})$ with internal parameters θ is employed, noting that a similar formulation is possible in the frequency domain.

The power of this approach comes from using a simple neural network, usually a shallow Dense Network (DN) that does not explicitly depend on γ , endowed with desirable properties through the judicious choice of a cost function. The cost should incorporate the governing equations and all available initial and boundary conditions. As an example in the frequency domain, consider the Helmholtz equation. Based on eq. (2), a term of the form

$$\left\| (\nabla^2 + k^2)(\tilde{u}_\theta) + \tilde{s} \right\|^2 \quad (7)$$

can be included in the cost function. Significantly, eq. (7) is expressed in a continuous format, underscoring that \tilde{u}_θ is a solution to the differential equation everywhere in the computational domain (ω, \mathbf{x}) . In practice, a small set of representative points is chosen to evaluate eq. (7) at. This acts as a regularizer for the data fidelity term $\|\tilde{u}_\theta(\omega, \mathbf{x}) - \tilde{p}_{\text{rec}}(\omega, \mathbf{x})\|^2$. Similar terms can be formulated for the initial and boundary conditions, or these can be learned implicitly if enough data is available.

In the case of inverse problems, the parameter $\gamma = k$ can be replaced with a neural network $\Psi_\phi : (\omega, \mathbf{x}) \mapsto k(\omega, \mathbf{x})$ with internal parameters ϕ . After an initial training stage for \tilde{u}_θ with data from a known reference medium, one can then train \tilde{u}_θ and Ψ_ϕ simultaneously from measurement data of the object of interest by considering the problem

$$\operatorname{argmin}_{\theta, \phi} \left\| (\nabla^2 + \Psi_\phi^2)(\tilde{u}_\theta) + \tilde{s} \right\|^2 + \lambda \|\tilde{u}_\theta - \tilde{p}\|^2 \quad (8)$$

with possible additional terms accounting for boundary and initial conditions. An example of this approach can be found in [84], where PINNs are employed in the estimation of speed of sound maps to locate cracks with high accuracy based on time domain data.

The tomography and FWI approaches discussed in this section can roughly be categorized as shown in table 9.

3.3. Ultrasound Data Classification

In the NDE 4.0 era, the fusion of DL and ML with ultrasound defect classification has markedly enhanced the performance and efficiency of industrial applications, resulting

in algorithms that are smarter, more robust and accurate, and more cost-effective. As with many data-driven methods, the success of classification methods in UT hinges on the availability and quality of training data [85]; the topic of data augmentation and synthesis is addressed in section 3.5. This section aims to provide an overview of recent advancements in ultrasound classification within NDE, highlighting works that integrate feature extraction with classification techniques. Feature extraction is critical in ultrasound, where sound data can be represented in various ways. This step quantifies key data characteristics, aiding classification algorithms in accurately distinguishing between classes. The effectiveness of combining signal processing methods, such as time-frequency-scale signal representations and dimensionality reduction, with DL networks and ML classifiers, is demonstrated in the examples provided.

The Short-Time Fourier Transform (STFT) and wavelet transform, providing simultaneous time and frequency domain information of signals, are integral in ultrasound classification for feature extraction [86]. Despite STFT being a traditional technique, its recent applications in NDE, specifically in structural health monitoring of railway tracks using CNNs, are notable [87]. Regarding the identification of rail defects, the wavelet transform has also proved to be a valuable tool for feature extraction. In [88], wavelet coefficients, energy, and local entropy are utilized for extraction of the representative features of the data alongside Kernel Principal Component Analysis (KPCA) for the dimensionality reduction algorithm. The authors of [88] propose utilizing SVM in the classification task. In [89], three ML classification techniques, in particular adaptive boosting [90], XGBoost [91] and SVM [92], are compared by accompanying wavelet energy features for classifying the defects with laser ultrasound signals.

Addressing another crucial NDE subsector, in [93], Discrete Wavelet Transform (DWT) is applied in a pipeline weld inspection using EMAT. The high-level features from the time-frequency representation of A-Scan signals are used to classify the welding defects in a gas pipeline. The wavelet features are then given into a CNN-SVM classifier. Different solutions to the problem of classifying ultrasound signals in welding applications are proposed in a similar manner by employing the wavelet coefficients-based extracted features in [94] with Artificial Bee Colony (ABC)-SVM and in [95] with CNNs. Another efficient implementation combining the extracted wavelet coefficients and CNNs is presented in [96] and [97] for identifying and monitoring the cracks in concrete, respectively.

The impact of the wavelet decomposition on classification accuracy is demonstrated in [98] by comparing two methods: one using Long Short-Term Memory (LSTM) [99] directly on the ultrasonic signals, and the other one applying LSTM after the wavelet feature extraction carried out. Yet another strength of the wavelet transform is extracting definitive features so that they can be used with unsupervised machine learning algorithms such as Gaussian Mixture Modeling, Mean Shift Clustering, and K-means Clustering [100]. Furthermore, apart from taking the wavelet coefficient-based values directly as

features, the usage of wavelets in reliable feature extraction can be utilized as a preprocessing step as well. In [101], the wavelet transform is carried out to denoise data in the context of detecting the possible damages in wind turbine blades.

Wavelet-based feature extraction is diversified through methods like Empirical Wavelet Transform (EWT), which adaptively decomposes signals into a finite number of components without requiring prior time-frequency information [102]. The authors illustrate the combination of EWT with CNNs for classifying phased array ultrasonic test signals. EWT draws inspiration from Empirical Mode Decomposition (EMD), a method for empirically deconstructing data into intrinsic oscillatory modes, capturing local time-scale signal information [103]. EMD was applied alongside DWT and other features, like entropy and crest factor, for acoustic emission signal-based wood damage and fracture classification, using LDA for classification [104]. Additionally, Variational Mode Decomposition (VMD) distinguishes itself by decomposing ultrasound signals through a non-recursive, constrained variational problem-solving approach [105]. VMD has been applied in ultrasonic measurement classification, such as in wood hole-damage [106] and for signal denoising prior to feature extraction [107].

Ultrasound signals, when represented sparsely using spatial sparsity and dictionary matrices [33], show promise in classification accuracy. The authors demonstrate this by replacing traditional iterative sparsity-promoting algorithms with a CNN for classifying low-quality, sparse reconstruction data [108]. This transformation involves a simple projection from the measurement to the image domain. The CNNs, configured in various architectures like LeNet-5 [109] and CaffeNet [110], outperforms the Smashed Filters algorithm [111], which uses Maximum Likelihood Estimator (MLE) for manifold classification, in terms of accuracy.

Shifting from signal processing to purely data-driven methods, a study [112] applies a Fully Convolutional Neural Network (FCN) and a Gated Recurrent Unit (GRU) for feature extraction in ultrasound signals, followed by a softmax layer for classification. The authors of [113] employ an autoencoder to discern defect-free signal characteristics and identify anomalies upon defect presence. In contexts where ultrasound data is sparsely represented, the authors demonstrate that classifying compressed or subsampled data using soft-margin SVMs, yields results as accurate as those obtained using the original fully sampled data [114]. Notably, this approach obviates the need for data reconstruction, significantly reducing computational complexity, particularly when the original data size substantially exceeds the subsampled one.

Last but not least, a comprehensive analysis of the recent enhancements in NDE with ultrasound data using numerous DL techniques utilized as feature extraction methods, such as autoencoders, GRUs, Recurrent Neural Networks (RNNs), CNNs is discussed in [115].

3.4. Dictionary Learning

In ultrasound imaging inverse problems, selecting an appropriate dictionary for the input data is crucial in finding

low dimensional representations of data, as well as in inverse problems such as imaging and denoising. Dictionaries can be designed by reducing the mutual coherence of the dictionary matrix, through standard optimization, or via learning techniques.

The k -SVD [116], a prominent method for dictionary optimization, is based on Singular Value Decomposition (SVD). It employs an alternating minimization approach, updating one dictionary matrix column and one data matrix row sequentially, while keeping other variables fixed. Notably, the k -SVD employs an approximate error matrix for updating the column of the dictionary matrix, rather than the actual one. In the study [117], this limitation is addressed in the context of sparsifying ultrasound elastography images by using the first principal component from the actual error matrix's Principle Component Analysis (PCA), in contrast to the k -SVD's use of the approximate error matrix's SVD.

Wavelet-based representation images is common in UCT and Magnetic Resonance Imaging (MRI), but the search for suitable dictionaries is ongoing since images synthesized from wavelets are not necessarily in the category of natural images. In [118], authors explore a better dictionary representation for ultrasound tomography and MRI. They employ an optimization method based on [119], which is an iterative alternating minimization method based on the loss function of the basis pursuit denoising problem. This method alternates between fixing the dictionary matrix and the image data, resulting in a 2dB improvement in PSNR level.

3.5. Synthetic ultrasound data

The generation of synthetic data increasingly attracts interest in NDE applications such as UT. On one hand, the validation of inspection procedures through sizing and classification of defects as well as Probability of Detection (PoD) requires large amounts of measurement data representing various types of inspection modalities and defects [120]. On the other, the training of ML models requires volumes of labeled data pertaining to a particular application which in practice are difficult to obtain. This section discusses the augmentation and synthesis of measurement data using AI techniques.

Pyle explored uncertainty quantification in DL for ultrasonic crack characterization, employing a CNN to assess surface-breaking defects in PWI images [121]. Two uncertainty quantification methods were applied: deep ensembles and Monte Carlo dropout. The network, trained on 14,343 simulated PWI images of surface-breaking defects generated via a hybrid Finite Element (FE)/ray-based model, was further calibrated using a mix of simulated and experimental images. Their findings indicated that while Monte Carlo dropout showed limited effectiveness in uncertainty quantification, deep ensembles demonstrated superior calibration and anomaly detection capabilities. Enhancements to deep ensembles, including spectral normalization and residual connections, further improved calibration and the detection of out-of-distribution samples. Additionally, Gantala explored crack detection using six synthetic Total Focusing Method

(TFM) imaging datasets, created through a combination of Finite Element Method (FEM) simulation, GAN-based methods, and realistic noise extracted through the sliding kernel approach, to enhance an Automated Defect-Recognition (ADR) in butt-welds [122]. Utilizing a fine-tuned pre-trained YOLOv4 network [123], they achieved a 100 % PoD in defect detection and less than 10 % false-calls on the hybrid dataset without noise, and 90 % PoD with less than 17 % false-calls on the noisy dataset.

Posilovic applied GANs to create ultrasonic images that mimic real ones, using a dataset of scanned steel blocks with artificially induced defects [124]. This dataset consists of 3825 images, comprising a total of 6238 annotations and 4283 defect patches after manual filtering. They explored three synthetic image generation methods: two deep learning-based GAN approaches and a traditional copy/paste technique. The first GAN method, detectionGAN, is a U-Net generator integrated with two PatchGAN discriminators [125] and a pretrained YOLOv3 [126] object detector. The second method, SPADE GAN [127], modifies the pix2pixHD [128] architecture by incorporating a pretrained YOLOv3 discriminator. Their methods were assessed through tests conducted by highly trained human experts.

Furthermore, Singh [129] and Ni [130] presented novel applications of generative AI in ultrasound imaging and elasticity modulus identification, respectively. Singh developed a DNN framework for real-time super-resolution mapping in ultrasonic non-destructive evaluation, using full aperture and pitch-catch transducer configurations to reconstruct crystallographic orientation maps. They employed a GAN with a U-Net generator and PatchGAN discriminator, achieving a fourfold increase in resolution and up to 50 % improvement in structural similarity. Ni focused on solving the inverse problem in elasticity, utilizing a conditional generative adversarial net to create shear modulus distributions from strain images. Their approach involved a U-Net architecture to implement a conditional GAN generator [131], and a PatchGAN classifier for discrimination.

Alternatively, since ultrasound propagation obeys physical laws, solving the wave equation (1) is another approach for UT data synthesization. Given a reference speed of sound distribution $c(\mathbf{x})$ and proper boundary conditions, the solution to the wave equation corresponds to the data that would be measured from the corresponding specimen. Conventionally, Partial Differential Equations (PDEs) including wave equations are solved using classical numerical methods such as finite elements or spectral approaches [122, 121]. Due to their robustness and sophisticated algorithms, such numerical methods play crucial roles when it comes to data synthesization. Yet, their high computational cost may become prohibitive especially when dealing with a large 3D region. Since the object surface needs to be specified, dealing with complicated geometry is also challenging with such numerical methods.

Outside of their applications in inverse problems such as FWI and UCT, PINNs have also shown significant promise purely in forward modeling, i.e. in enhancing

numerical methods for solving the wave equation [81]. Moseley demonstrated that a simple 10-layer shallow MLP can effectively simulate 2D wave propagation in inhomogeneous media [82]. Song tackled the challenge of balancing physics and boundary loss in PINNs by integrating perfectly matched layers into the Helmholtz equation, achieving impressive results in inferring 2D wave fields with anisotropic wave speeds in inhomogeneous media [132]. Often explored a variational approach to PINNs, successfully inferring 1D wave propagation in a homogeneous medium with reflective boundaries [133]. This approach reformulates a second-order PDE as a first-order differential equation, providing an effective alternative for time-domain wave equation solutions. For a comprehensive overview of PINNs, the review by Karniadakis is recommended [134].

4. Thermography

Infrared thermography has established itself as a valuable technique in non-destructive evaluation due to its ability to provide prompt, swift, and cost-effective information. We will explore both state-of-the-art conventional methodologies and their AI-based counterparts in this field. Leveraging AI, thermography effectively eliminates blurring and reconstructs initial temperature profiles. A pivotal focus is defect detection using DL architectures, discussed comprehensively in this section.

4.1. Pulsed Phase Thermography

Pulsed Thermography (PT) [135] is one of the popular stimulus methods of Thermographic NDE (TNDE). The specimen undergoes a pulse of external thermal stimulus, and the resulting temperature decay is captured by an Infrared (IR) camera. This pulse of energy can be generated using high-power amplifiers, flash lamps, laser beams and water jets. The setup can be deployed in two modes: reflection and transmission. In reflection mode, both the source and the detector are positioned on the same side of the sample. In contrast, in transmission mode, the source and detector are located on opposite sides of the sample to be inspected. The effectiveness of this method varies based on the pulse duration, ranging from a few milliseconds for materials with high thermal conductivity, such as metals, to a few seconds for materials with low thermal conductivity, like wood. This allows for the inspection of different materials using the TNDE approach.

In a qualitative assessment, when a pulse is applied to the specimen, its temperature rises during the application of the pulse. Subsequently, the temperature decreases as a thermal front propagates beneath the surface, following the principles outlined in the Fourier diffusion equation, which is given by

$$\frac{\partial T}{\partial t} = \alpha \nabla^2 T. \quad (9)$$

Here, $\frac{\partial T}{\partial t}$ is the rate of change of temperature with respect to time, α is the thermal diffusivity of the material and $\nabla^2 T$ represents the Laplacian of the temperature field,

indicating how temperature varies spatially. The presence of subsurface defects modifies the diffusion rate, resulting in temperature variations above these defects when compared to the surrounding undamaged areas. Consequently, thermal differences can be detected in thermal images above defect areas. Moreover, the diffusion rate is time-dependent, leading to delayed and less pronounced manifestations of deeper defects. The expressions

$$\begin{aligned} t &\propto \frac{z^2}{\alpha} \\ c &\propto \frac{1}{z^3} \end{aligned} \quad (10)$$

establish the relationship among the observation time t , the thermal contrast c , the defect depth z , and the thermal diffusivity α .

In Pulsed Phase Thermography (PPT) the sample is stimulated as in PT technique whereas the analysis is similar to Modulation Thermography (MT) technique [136]. In this scenario, a brief rectangular heat pulse is applied to the sample, and its reaction is observed through an infrared camera. This pulse has a wide range of frequencies, which can be separated using the Fourier transform. The data analysis involves choosing a specific frequency, akin to synchronizing the output signal with the modulated input signal, similar to the process in MT. The Fourier transform of every pixel (i, j) in the imaging array is then computed along time domain axis.

The energy of the stimulating pulse is primarily concentrated in the lower frequency range of the spectrum. According to eq. (10), lower frequencies can penetrate deeper, while higher frequencies are confined closer to the surface. Hence, it is appropriate to select lower frequencies for analysis. Additionally, it has been observed that the phase image remains unaffected by the surface properties of the material and the non-uniformity of the source, unlike the amplitude image. However, in PPT analysis, time information is lost while retrieving frequency data. Combining time information with frequency data can be immensely valuable for depth estimation analysis. Advanced techniques such as wavelet analysis, neural networks, synthetic data, and statistical methods can be employed for such analyses.

In the current literature, investigations have been conducted to detect and evaluate defects by modifying the PPT algorithm. In [137] two modified algorithms were introduced. The first algorithm integrates a frequency-dependent Gaussian window function, while the second algorithm utilizes a rectangular window function. The algorithms underwent testing using synthetic signals that modeled a subsurface cylindrical defect in a plate, and experimental testing was conducted through PT on steel and a polymer sample. The outcomes revealed a notably improved contrast-to-noise ratio for defects, particularly at higher analysis frequencies.

In the general context, PPT necessitates the assessment of multiple-phase images at various frequencies for a comprehensive sample evaluation. However, the selection and subsequent evaluation of these images are encumbered

by certain challenges and are not always straightforward. In efforts to ameliorate these limitations, [138] introduced an Adaptive Spectral Band Integration (ASBI) processing technique. This approach surpasses the capabilities of PPT, yielding an enhanced signal-to-noise ratio even for defects that are barely visible. Furthermore, it produces a single index map of defects for a given sequence, simplifying the interpretation process.

4.2. Principal Component Thermography

PCA is a widely used multivariate statistical technique designed to reduce the complexity of data. Through linear transformations, PCA identifies the key features within high-dimensional data and maps them onto a lower-dimensional space. This approach offers several advantages, including straightforward implementation, feature extraction, and noise reduction.

In the realm of Infrared Thermography (IRT), Principal Component Thermography (PCT) [139, 140, 141] employs a method involving the singular value decomposition of the covariance matrix derived from thermograms. This process effectively reduces the dimensions of thermographic data and captures significant data changes. Simultaneously, by projecting the original data onto the directions of maximum variability, PCT efficiently diminishes noise present in the thermographic data.

Replying solely on PCT may not yield satisfactory results. Consequently, numerous defect inspection methods based on deep learning have been proposed in recent times. One such advancement is the Spectral Normalized GAN (SNGAN) algorithm [142]. The complexity of the generator (G) and discriminator (D) in traditional GANs often leads to challenges like vanishing or exploding gradients during training. The SNGAN tackles these issues by incorporating spectral normalization, a technique that normalizes the weight matrix in the discriminator [143]. This approach confines the spectral radius of the weight matrix within a fixed range, effectively preventing issues like gradient disappearance or explosion. By implementing this normalization, the training stability of GANs is significantly enhanced, leading to the generation of higher-quality images. The architecture of the SNGAN-based generative principal component thermography (GPCT) model is depicted in fig. 5. In this proposed approach, the traditional PCT method involves combining the generated images with the original thermal images, followed by PCA data analysis.

This integration enhances the overall defect detection process and ensures more accurate and reliable results.

4.3. Thermographic Signal Reconstruction

Originally developed for pulse thermography, the Thermographic Signal Reconstruction (TSR) processing technique [144] consists in the fitting of the experimental log-log plot thermogram by a logarithmic polynomial of degree n . Using $\Delta T = \Delta T(t)$ to represent the temperature increase as a function of time (thermogram) for a single pixel (i, j) , the

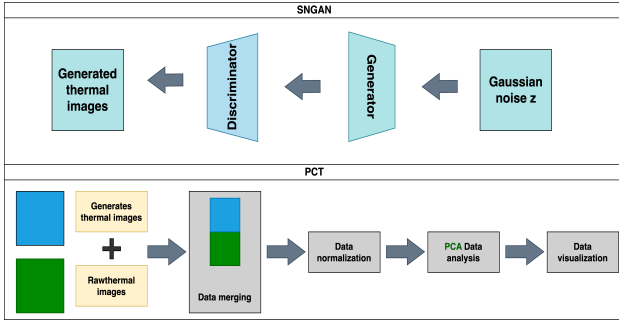


Figure 5: Framework of the GPCT model.

temperature increase is modelled as

$$\log_{10}(\Delta T) = a_0 + a_1 \log_{10}(t) + a_2 \log_{10}(t)^2 + \dots + a_n \log_{10}(t)^n. \quad (11)$$

This fitting method replaces the entire sequence of temperature rise images $\Delta T(t)$ with a series of $(n+1)$ images \mathbf{A}_m , $0 \leq m \leq n$, representing the polynomial coefficients, so that $\mathbf{A}_m(i, j)$ is the m th coefficient at pixel (i, j) . These coefficients facilitate the reconstruction of an entire thermographic sequence. The computation of the initial and subsequent logarithmic derivatives of the thermograms is directly conducted on the polynomial, leading to minimal temporal noise augmentation.

The procedures for fitting and deriving thermograms depend on the specific temporal domain being analyzed. It's essential to define a precise time window to isolate the segment of thermograms affected solely by the particular physical phenomena under examination. The traditional use of TSR involves selecting optimal derivative images corresponding to distinct depth ranges. Empirically, from [145] it was determined that a degree of $n = 11$ adequately represents delamination-like defects.

In a few recent studies, Schager et al. [146] investigated an expanded TSR method aimed at automatically categorizing defects found within the undamaged domain. The approach creates defect maps by utilizing the signal attributes of flaws. The results of the research suggest that the defect map offers an estimate of the defect's depth and is computationally efficient.

Feng et al. [147] introduced a hybrid approach that combines TSR with the Automatic Seeded Region Growing (ASRG) algorithm for thermal image signal processing. The study emphasizes that the selection of defective regions is sensitive to high image resolution, which can enhance detectability. The study showcased enhanced detection resolution and proved valuable for automatically selecting regions suspected of harboring defects. Ratsakou et al. [148] proposed a novel approach for defect characterization, blending TSR with the Canny shape-reconstruction algorithms. The method begins by fitting the raw thermographic images to a low-degree polynomial in the log-log representation of the time axis. Subsequently, the Canny algorithm is employed to reconstruct the original signals. By harnessing the capabilities of the TSR algorithm for signal denoising and compression, the method can improve the efficiency of the reconstruction process.

4.4. Thermographic Image Reconstruction

The techniques mentioned in the preceding sections do not exploit spatial information and physical knowledge of the problem simultaneously, resulting in limited spatial resolution. In the case of TSR, each pixel is traditionally processed separately. In PCT, spatial information is considered only in the context of forming low dimensional vector spaces. An alternative approach is to perform thermographic image reconstruction by directly addressing the heat equation in (9) and solving an Inverse Heat Conduction Problem (IHCP) to find the initial temperature distribution in the object under test. Such an approach is comparable to FWI in ultrasound imaging and comes with similar challenges, e.g. considerable computational cost and ill-posedness [149].

A recent advancement in thermographic imaging is the transformation of the heat conduction problem into a wave propagation one by means of virtual waves [150], after which the usage of the reconstruction techniques covered in section 3 becomes possible. In particular, synthetic aperture techniques address both the limited spatial resolution of TSR and PCT, as well as the ill-posedness of IHCPs: the incorporation of a simplified model of wave propagation provides robustness and improves to spatial resolution. The inverse mapping from the measured temperature profile $T(t, \mathbf{x})$, $\mathbf{x} \in \mathbb{R}^d$, to the desired initial temperature distribution $T(0, \mathbf{x})$ is performed through an intermediate virtual wave field $p(t, \mathbf{x})$. Classical and AI-based methods can be employed at any step of the process, resulting in increased flexibility. The authors of [151] exemplify this flexibility by comparing three approaches to thermographic imaging: virtual waves with classical ultrasound imaging methods, an end-to-end U-net $\Psi : T(t, \mathbf{x}) \mapsto T(0, \mathbf{x})$, and a two-step approach in which the virtual wave mapping $T(t, \mathbf{x}) \mapsto p(t, \mathbf{x})$ is done in preprocessing and later fed to a neural network $\Psi : p(t, \mathbf{x}) \mapsto T(0, \mathbf{x})$. The authors show that both AI-based approaches outperform the classical one, and that the usage of virtual waves in preprocessing increases reconstruction accuracy in exchange for increased inference cost.

4.5. Defect Shape Detection

Neural networks for semantic segmentation prove valuable across diverse tasks, such as autonomous vehicles, medical image diagnostics, and other combined applications [152, 153]. In the case of thermographic imaging, semantic segmentation allows the detection and localization of abnormalities, e.g. tumors in medical imaging [154] and defects in NDE [155].

In [156], semantic segmentation is performed on induction PPT images of forged steel parts by using a U-net. The network is trained by using binary masks denoting the presence and location of cracks. The authors note that, since the cracks are comparatively small in the Region of Interest (ROI), imbalances in the classes must be addressed through weighting in the loss function. As is common in the NDE context, augmentation through rotations, contrast modifications, and elastic transformations was necessary.

5. Optical Camera

A significant fraction of NDE tasks can be solved through optical inspection methods, i.e., based on optical sensors using image processing methods. Such optical systems can consist of cameras, lasers, scanners, or a combination of the above. However, machine vision with a camera is the most common. Figure 6 shows the typical workflow of a camera system [157].

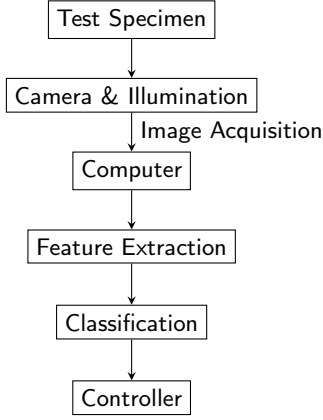


Figure 6: Setup of a camera system

A camera and a suitable (active or passive) illumination are used to take one or multiple images of the specimen, which are subsequently transferred to the computer. The image matrix \mathbf{P} for a grayscale image can be represented as $m \times n$ matrix where each entry $\mathbf{P}(i, j)$ represents the brightness value of the pixel located at the i -th row and j -th column of the image. For color images, each color plane is described like this and written into a three dimensional array. Afterwards, feature extraction is applied. Feature extraction in an image can be mathematically represented as a function $f(\mathbf{P})$ that transforms the original image into a set of features or vectors:

$$f(\mathbf{P}) = \{f_1, f_2, \dots, f_k\} \quad (12)$$

Here, f_1, f_2, \dots, f_k represent the extracted features. These features can be of various types, depending on the type of analysis. In NDE, relevant features could be e.g. the edges of a scratch, certain color characteristics indicative of corrosion, etc. Then the data can be classified. The classification process can be mathematically represented as a function $c(f(\mathbf{P}))$ that maps the features to a specific class or label:

$$c(f(\mathbf{P})) \in C \quad (13)$$

Here, C is the set of all classes under consideration, and c yields a class or label for the image or region based on the extracted features. According to the above examples, the question can be clarified whether, for example, the edges found have the characteristics of a scratch, or whether the color features found correspond to those of corrosion. After the data evaluation, the process chain ends with a controller, which makes a certain decision depending on the class.

Nowadays, thanks to the advanced development of neural networks, many of these problems can be solved via Deep Learning. A simple scheme is shown in fig. 7.

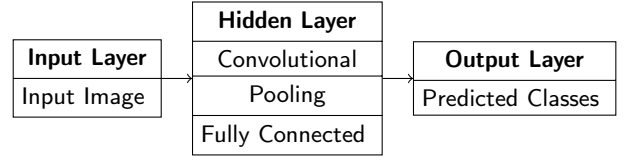


Figure 7: Convolutional Neural Network (CNN) Architecture

In the example, the input image goes through many different convolution operations, a common approach in image processing to establish shift invariance of detected objects across the image. During this process, corresponding feature maps are created. The feature maps are compressed by the pooling layer. The fully connected layer connects the different maps so that the desired classification is obtained in the end.

5.1. Image Preprocessing

Image preprocessing means the intention to achieve image enhancement in conjunction with formatting the image if necessary. Such operations could include smoothing the image, adjusting the contrast, resizing the image, formatting in a different color range, eliminating the background and more. The various operations depend very much on the actual application. This section briefly introduces the most common operations in general. For deep learning, image preprocessing is essential for technical, qualitative and performance reasons.

Smoothing filters [158] are used to suppress noise and individual disturbing pixels. A distinction is made between linear and non-linear filters. Linear smoothing filters [158] can be described as

$$\mathbf{G}(x, y) = \frac{1}{s} \sum_{r=0}^{R-1} \sum_{c=0}^{C-1} f_{cr} \mathbf{P}(x - d_x + c, y - d_y + r), \quad (14)$$

where $\mathbf{G}(x, y)$ is the filtered image at position (x, y) , $\mathbf{P}(x - d_x + c, y - d_y + r)$ is the pixel value of the input image at position $(x - d_x + c, y - d_y + r)$, which is weighted by the filter coefficient f_{cr} . The quantity s is a normalization constant and d_x and d_y are parameters which control the size of the filter. R is the number of rows and C the number of columns in the image. The row and column indices are represented by r and c , respectively.

Non-linear smoothing filters [158] are 'Rank-Order Filters'. Here, a certain number of neighboring pixels are sorted into a row depending on their intensity. A specific pixel is then selected. A common Rank-Order Filter is the so-called Median filter [158], which always selects the median intensity and thus makes disturbing pixels disappear completely.

Regarding image enhancement, there are many different ways to improve the contrast of images. A general solution for this is the so-called histogram normalization which can be

described via

$$\mathbf{G}(x, y) = \frac{L-1}{MN} \sum_{i=0}^{L-1} h(i) \quad (15)$$

where $\mathbf{G}(x, y)$ is the enhanced image, L is the number of intensity levels, M is the image width and N the height. Additionally, $h(i)$ is the count of the i -th intensity in the original image. For color images, these procedures are carried out for each individual color plane.

Moreover, for deep learning, image resizing is very important, as neural networks need the input images in to be in a homogeneous format. By a scaling factor s the dimensions of the resized image can be calculated based on the original image. Then by applying an interpolation technique the old pixel coordinates can be mapped into the new image coordinate system.

As fully connected layers in convolutional neural networks require the same format for all images, also a color transformation may be necessary. In general we can describe it as follows

$$\mathbf{G}(x, y) = \mathbf{T}[\mathbf{P}(x, y)] \quad (16)$$

\mathbf{T} is the transformation function which applies a transformation to the color values of each pixel. The transformation function can be defined based on the requirements of the wished color format.

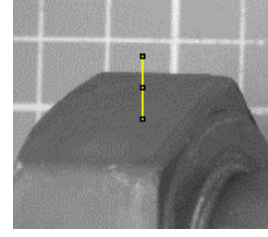
5.2. Feature Extraction and Classification of Optical Images

The first step in feature extraction is to define a region of interest in which to search for the desired features. This can be achieved, for example, using threshold methods, edge detection techniques or cluster algorithms. Representative features that characterize the image content are then selected. These can be color information, edges, shapes, textures or specific patterns. The extracted features are then described as a vector as in eq. (12). The vectors are then filtered again to reduce the amount of data or to discard irrelevant features. Finally, the vectors may also need to be normalized to make them comparable. Then the extracted features can be analyzed so that based on the application the images can be classified.

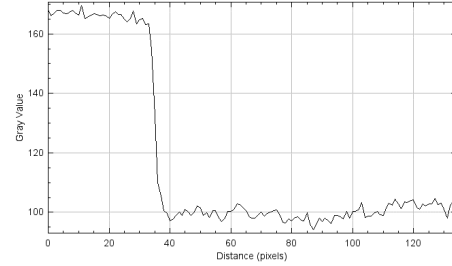
Figure 8 exemplifies feature extraction in optical images by considering a section of the head of a screw. A line is plotted here and the adjacent graphic shows the corresponding line profile. The corresponding drop in intensity from the line function represents the edge of the object and so a corresponding feature can be extracted. If the entire screw is scanned in this way, the contour of the object can be determined and the object can be classified as a screw accordingly. In the context of Deep Learning, CNNs can be trained to register such patterns automatically. In the following subsection, we review the application of DL to optical images in detail.

5.3. Deep Learning based Feature Extraction and Classification

Deep learning was revolutionary in image processing. By training neural networks, they can acquire an intuition



(a) head of screw



(b) line profile

Figure 8: Example of feature extraction

that is similar to humans' and thus solve highly complex tasks. Image files are usually processed with convolutional neural networks. These networks are predestined for extracting features from images and then classifying them. Tasks such as object recognition, segmentation, finding key points and much more can be easily solved using convolutional neural networks.

There are many different architectures for this, Region Based Convolutional Neural Networks (R-CNNs) [159] among them. A Region Proposal Network (RPN) is used to find regions that are likely to contain objects. A CNN architecture is then used to classify and fine-tune the bounding boxes. Ren et. al [160] introduces the Faster R-CNN. They use as CNN architecture the VGG-16 [161] for the classification. They tested it on the PASCAL VOC 2007 and 2012 [162] dataset. The best results were achieved when the model was trained with the COCO dataset [163] and the PASCAL VOC 2007 and 2012 dataset. For the VOC 2007 test data a mAP of 78.8 % were achieved and for the VOC 2012 test data the mAP amounted to 75.9 %.

Another architecture is Single Shot MultiBox Detector (SSD) [164]. This model uses the VGG-16 architecture as base, but disposes of the fully connected layers. Instead of these, further convolutional layers are added so that several feature maps with different resolutions can be generated. All these maps are taken into account for classification. This not only makes it possible to reliably find and classify the objects, but also to match the object shape when generating the bounding boxes due to the large number of feature maps at different levels. Liu et. al [164] introduced this model. In their paper they differentiate between SSD300 and SSD512, where the number indicates the input size of the images (300x300 vs 512 x 512). Here too, the models were tested with the PASCAL VOC 2007 and 2012 dataset. Again the best results were achieved if the models were trained with the VOC 2007,

VOC 2012 and COCO dataset. The SSD300 achieved a mAP of 79.6 % for the VOC 2007 testset and a mAP of 77.5 % for the VOC 2012 testset. The SSD512 achieved better results due to the higher resolution of the input images. For the VOC 2007 data the mAP amounts to 81.6 % and for the VOC 2012 testset it is 80.0 %.

A widely used method for real-time object recognition is YOLO [165]. Here, the image is divided into grids and a prediction is made for each grid. YOLO is based on CNNs (see Figure 7). In 2015, Redmon et al. [166] introduced YOLO for the first time. They trained the model with the VOC 2007 and 2012 dataset. For the VOC 2007 data it then achieved a mAP of 63.4 %- and for the VOC 2012 dataset the YOLO scored 57.9 % mAP. Over the years, new and improved versions of YOLO were published. YOLOv8 [167] is the latest release. The largest version of the model (YOLOv8x) achieved the best results. It was trained with the COCO 2017 dataset and achieved a score of 53.9 %. Moreover YOLOv8 also provides models which perform only classification (without bounding boxes), instance segmentation and pose estimation.

In addition to object recognition, image segmentation is also often required. This can be achieved by extending the object recognition models. An example of this is Mask R-CNN. Mask R-CNN [168] [159] is an approach to Instance Segmentation. It uses the Faster R-CNN [160] [159] architecture for object detection and a FCN [169] for semantic segmentation. He et al. trained and tested a Mask R-CNN model with the COCO dataset. The model reached a score of 37.1 AP. In comparison to that the YOLOv8x-seg model achieved a mAP score of 43.4. This model was trained and tested with the COCO 2017 dataset.

All these applications are extremely valuable in NDE tasks. For instance in Katsamenis et. al [170], corrosion detection is carried out. Among other models, Mask R-CNN is used here. Transfer learning was used to train the Mask R-CNN model. The Mask R-CNN model is based on Inception V2 [171] and was pre-trained on the COCO dataset. Then a dataset consisting of 116 images was used to train and test the model. The images were captured using various devices and have different resolutions. Furthermore, the images contained different types of corrosion. The precision achieved was just under 0.7 and the F1-Score achieved was just over 0.7. However, the results were improved by combining them with color segmentation to apply boundary refinement. This shows the importance of classical techniques such as those in Section 5.2 in order to combine AI results with such procedures if necessary.

6. Common Patterns in Algorithms and ML Models

So far we presented both classical and ML based approaches separately for each inspection modality. In the course of investigation, however, we repeatedly encounter some algorithms and/or ML architectures regardless of the inspection modalities or even application fields. For instance, CNNs are ubiquitously employed for computer

vision based decision making tasks in many inspection modalities including the ones that are not covered in this paper: defects and/or substance classification in UT [87, 93] and terahertz inspection [172], edge detection in X-ray [173] or semantic segmentation in thermography [155], feature extraction and classification in optical images [174] and X-ray tomography [175, 176]. Often integrated as a part of feature extraction, CNNs can also be used for imaging tasks such as for reconstructing the raw terahertz measurement data [177, 178] or enhancing the resolution of UT [179, 180] and X-ray reconstructions [177, 178]. Such ubiquity can also be found for classical algorithms as well. An example is correlation based imaging, which is however called differently depending on the applications: SAFT and TFM for UT, Synthetic Aperture Radar for radar and DAS beamforming for medical ultrasound.

All these examples make it evident that there are common patterns in how to process the data depending on the tasks instead of inspection modalities or application fields. One can find such patterns, when these tasks deal with the intrinsically same mathematical problems. As a result, these tasks can be formulated mathematically in the similar, if not the same, manner. For example, reconstructing the inner structure of a test object from UT signals can be formulated in a very similar manner as that of reconstructing X-ray Computed Tomography (CT) data or image deblurring [181]. This is because all of these tasks aim to recover the quantities which cannot be observed directly from the observations that are affected by these unknown quantities. To be more specific, these unknown quantities can be the location of defects in a test object for UT or X-ray reconstruction, and the unknown clean image for deblurring tasks. This realization motivates us to make high level connections of the references in terms of their intrinsic natures. For this purpose, we identified four intrinsic mathematical problems we commonly encounter in NDE applications, which are *forward problems*, *inverse problems*, *optimal design* and *pattern recognition*.

In the following subsections, each problem is described to help identify the intrinsic nature of a specific engineering task. The emphasis is placed on the common patterns one can see when dealing with these tasks. In table 10, some recommended references are provided as a summary of this section. The left most column shows the mathematical problems these references intrinsically solve. The specific NDE related tasks are listed in the second column. The third column of the table provides the list of the sections which discuss how these problems are solved for a specific inspection modality. The fourth column shows common methods to solve these tasks, and the fifth column is the list of references for the corresponding methods. Furthermore, these tasks are highlighted with four different colors to illustrate how they relate to actual NDE inspections. Inspired by the NDE automation levels proposed in [1], we decompose a NDE inspection chain into three steps: measurement operation, enhancement of raw measurement data and decision making. In addition to that, we consider data synthesization as an essential part of the future of NDE inspections, since there is a pressing need for high quality, well-labeled data for

reliable AI training. Admittedly, this is by no means an exhaustive collection, yet it will give a brief overview of how one can interpret and possibly solve these tasks regardless of applications. Note that the conceptual connections we made here is just one possibility, and they can be described and grouped differently.

The benefits of table 10 are twofold. First, acknowledging such conceptual patterns lets us understand the similarities in the tasks and try a method in other modalities or application fields. In the era of NDE 4.0, where high level problems need to be solved by machines instead of human operators, we will increasingly encounter the problems for which no state of the art exist. However, once the nature of the tasks is identified, such common patterns can help us determine which measure, algorithm and/or ML architecture is suitable. Second, the number of listed methods in table 10 also indicates which tasks are well investigated and which are still in its infancy. This can be useful for determining the direction of future research.

6.1. Forward Problems

For the purposes of this work, we refer to general problems of the form $\mathbf{y} = f(\mathbf{x})$, which shows a relation between the causal factors \mathbf{x} and their effects \mathbf{y} using an operator f . For the sake of simplicity, in this work we represent both \mathbf{x} and \mathbf{y} as vectors, however they can be arrays as well.

Forward problems seek to obtain the effects \mathbf{y} from the known causal factor \mathbf{x} . In the context of NDE, f usually represents a measurement process, yielding a synthesized version of measurement data \mathbf{y} . Especially for ML-based approaches, where the lack of quality data has been frequently identified as a major bottleneck regardless of their tasks [1], solving forward problem is beneficial as it can enlarge the training data set. For most cases with NDE applications, \mathbf{x} and \mathbf{y} are related through the underlying physical phenomenon described by a PDE, such as Maxwell's equations, wave or heat equations. Since solving these PDEs is typically very challenging, the true causal relation is generally approximated. As a result, there are various possibilities to select the operator f . For accurately computing \mathbf{y} , one can aim to find f such that it approximates the underlying PDE. Another approach is to simplify the PDE by making assumptions on the underlying physics, enabling to explicitly compute f to compute \mathbf{y} .

6.2. Inverse Problems

Given the causal relation $\mathbf{y} = f(\mathbf{x})$ we considered in the previous section, inverse problems aim to find the parameter \mathbf{x} from a set of observations \mathbf{y} collected through a (measurement) process f . For example, when f adds noise to \mathbf{x} so that \mathbf{y} is a noisy version of \mathbf{x} , the inverse problem is a denoising problem. If \mathbf{y} is an image and one seeks to increase its resolution, f can be interpreted as *subsampling* operation, and recovering \mathbf{x} becomes super-resolution task. In the case of imaging, we consider \mathbf{x} to be an *image* in the sense that it describes a parameter that varies in space, and the raw measurement data \mathbf{y} is defined in a different domain and/or cannot be interpreted as an image. As a concrete example, eddy current testing deals with the measurement of magnetic field intensity and

phase obtained with varying excitation frequencies. In the case of ultrasound, raw data often consists of time domain acoustic pressure signals collected with different measurement channels. For both, the data is processed to obtain an image portraying defect locations. In the case of inverse problems, NNs facilitate the computation of \mathbf{x} by replacing parts of classical algorithms to invert f , or replacing them entirely, i.e. $\mathbf{x} = \Psi(\mathbf{y})$, where Ψ is the NN. Typically, the quality of the inversion is measured through a cost function $h(\mathbf{x}, \Psi(\mathbf{y}))$ which we want to minimize, such as eq. (5).

6.3. Optimal Design

Optimal design deals with the tuning of experimental parameters which can be freely chosen, and which impact the information content of measurement data with regards to parameters of interest. Recall the inverse problem from section 6.2. In reality, the measurement data \mathbf{y} depends not only on \mathbf{x} , but also on the experimental parameters (e.g. the location, number, and type of sensors employed) ϕ . When solving an inverse problem, the achievable cost h is affected by the experimental design. We can tune the parameters ϕ so that the cost h is minimal, i.e. $\min_{\phi} h(f(\mathbf{x}, \phi))$.

6.4. Pattern Recognition

Pattern recognition can be found ubiquitously in many data analysis and decision making tasks. In general, given the input data \mathbf{x} , we would like to assign it a category or class y . There exists a correspondence between \mathbf{x} and y given by an unknown mapping g that we wish to find. Whether a category is assigned to \mathbf{x} as a whole, by regions, or by sample, provides the nuance among classification, detection, and segmentation, respectively. Oftentimes, the data \mathbf{x} is preprocessed through a judiciously chosen function f which highlights informative *features*. This leads to the overall pattern recognition task $y = g(f(\mathbf{x}))$ which renders itself to a problem of finding an appropriate classifier g , preprocessing scheme f , or both. NNs can be used to replace the classifier g in combination with classical feature extraction methods such as PCA, or they can replace both the feature extraction and classification process altogether. Since the learning is typically based on the available samples, the quality of the samples determines the performance.

7. Summary and Conclusions

In this paper we discuss the state of the art in a variety of NDE techniques. In light of the challenges brought about by the recent advances in the corresponding industries, significant technological advances in NDE are required. The discussion of the different NDE modalities has emphasized some of the intricacies we are facing. More often than not, a measurement device that is sensitive for a desired physical effect will also react to unwanted effects such as environmental operating conditions (e.g., temperature) or coupling effects (e.g., sensor lift-off). The complexity of the signals requires significant experience for their interpretation in order to detect subtle effects and recognize artefacts. Training is often hindered

| Intrinsic problem | Task | Section | Method | References |
|---------------------|---------------------|--|------------------|---|
| Forward problems | Data synthesization | 3.5, 4.2 | numerical solver | [122], [121] |
| | | | PINN | [81], [82], [132], [133] |
| | | | GAN | [122], [130], [124], [142] |
| Inverse problems | Imaging | 2.1, 2.2, 2.3, 2.4, 3.1.1, 3.1.2, 3.2, 4.3 | classical | [37], [38], [39], [71], [72], [74], [75], [182] |
| | | | MLP | [5], [13], [6], [7], [21] |
| | | | SVR | [26] |
| | | | HLR | [26] |
| | | | XGBoost | [25] |
| | | | CNN | [80] |
| | | | Autoencoder | [40], [183] |
| | Super-resolution | 3.1.1, 3.1.2, 3.2, 3.5 | PINN | [134], [81], [84] |
| | | | CNN | [80] |
| | | | U-Net | [78], [79] |
| Optimal design | Optimal excitation | 3.1 | classical | random ([33], [34]), optimized ([35]) |
| | | | DL | [36] |
| | Subsampling | 3.1.2 | classical | [64] |
| | | | DPS | [63] |
| Pattern recognition | Feature extraction | 2.1, 2.4, 4.2, 5 | unsupervised | PCA ([139]) |
| | | | supervised | LDA ([29], [28]), SVM ([114]), SVR ([9]) |
| | Classification | 2.1, 2.4, 3.3, 5.3 | classical | [28], [111] |
| | | | kNN | [29], [28] |
| | | | MLP | [15] |
| | | | Probabilistic NN | [10] |
| | | | CNN | [108], [87], [93], [97] |
| | | | YOLOv8-clc | [167] |
| | Detection | 2.1, 2.4, 5.3 | MLP | [14], [27] |
| | | | RBF | [12], [16] |
| | | | YOLOv4 | [123] |
| | | | YOLOv8 | [167] |
| | | | Faster R-CNN | [160] |
| | | | SSD | [164] |
| | Segmentation | 2.1, 5.3 | classical | [184] |
| | | | CNN | [156], [154] [155], [169] |
| | | | YOLOv8-seg | [167] |
| Mask R-CNN | | | [168] | |

Table 10

Summary of the methods used for common NDE tasks. References are categorized according to the intrinsic mathematical problem they are dealing with as discussed in section 6. Each color in the table is associated to a NDE inspection process: pink for data synthesization, green for data enhancement, orange for measurement operation and blue for decision making. Note that end-to-end ML methods often perform feature extraction implicitly. These methods are not shown as feature extraction, instead categorized into their targeted decision making tasks.

by lack of available labeled data, which is costly to generate. Finally, since each modality is very different, generic solutions are often not available or lack in efficiency due to insufficient incorporation of the physics of the problem and the sensors.

The paper has outlined a number of AI approaches for different NDE modalities, demonstrating examples where AI is already helpful today. In particular, we have shown that AI can assist us in detection (e.g., cracks, voids) and classification (e.g., material, defect type) as well as segmentation problems. Moreover, AI methods have been successfully applied in the estimation of parameters (e.g., crack depth/size, material parameters). In addition, AI methods can be a powerful tool for solving complex inverse problems for beamforming and imaging, even in complex situations such as Ultrasound

tomography where full waveform inversion methods are required. Of course, they can also be used for image quality improvement (e.g., deblurring, denoising, super resolution).

Often, such methods can be tailored to be robust against calibration issues such as variations in environmental operating conditions (e.g., temperature) or sensor coupling (e.g., lift-off). The lack of training data can sometimes be alleviated through synthetic data generation for which dedicated AI methods have been devised. An interesting thread of research is to use AI methods even very early, e.g., to assist in devising the optimal sensor placement and related design of experiment questions.

Overall, it is evident that AI methods have become indispensable tools for advancing the NDE field further.

We are certain that we are just witnessing the beginning of a research field that will give rise to even more powerful semi-automated NDE systems which are required to keep up with the digital transformation of our industries.

CRedit authorship contribution statement

Eduardo Pérez: Conceptualization, Writing - Original Draft, Writing - Review & Editing, Supervision. **Cemil Emre Ardic:** Writing - Original Draft. **Ozan Çakiroğlu:** Writing - Original Draft, Visualization. **Kevin Jacob:** Writing - Original Draft. **Sayako Kodera:** Conceptualization, Writing - Original Draft. **Luca Pompa:** Writing - Original Draft. **Mohamad Rachid:** Writing - Original Draft, Visualization, Writing - Review & Editing. **Han Wang:** Writing - Original Draft, Visualization. **Yiming Zhou:** Writing - Original Draft, Visualization. **Cyril Zimmer:** Writing - Original Draft, Visualization. **Florian Römer:** Writing - Original Draft, Writing - Review & Editing, Project administration, Funding acquisition. **Ahmad Osman:** Project administration, Funding acquisition.

Conflicts of Interest

The authors declare no conflict of interest.

Acknowledgements

This work was partially supported by the Fraunhofer Internal Programs under the grant Attract 025-601128, the Federal Ministry of Education and Research (BMBF) through the VISiMOS project with grant number 03VP10900, and the Thuringian Ministry of Economic Affairs, Science and Digital Society (TMWWDG).

Acronyms

kFCV *k*-Fold Cross Validation
kNN *k*-Nearest Neighbour
 R_e Yield Strength
 R_m Tensile Strength
 R^2 Coefficient of Determination
3MA Micromagnetic Multiparameter Microstructure and stress Analysis
ABC Artificial Bee Colony
ABLE Adaptive Beamforming by Deep LEarning
ADMIRE Aperture Domain Model Image REconstruction
ADMM Alternating Direction Method of Multipliers
ADR Automated Defect-Recognition
AI Artificial Intelligence
ANN Artificial Neural Network
ART Algebraic Reconstruction Technique
ASBI Adaptive Spectral Band Integration
ASRG Automatic Seeded Region Growing
CEUS Contrast-Enhanced Ultrasound
CNN Convolutional Neural Network
CNR Contrast-to-Noise Ratio
COBA Convolutional Beamforming Algorithms
CORONA Convolutional Robust Principal Component Analysis
CS Compressed Sensing

CT Computed Tomography
DAS Delay and Sum
DBTT Ductile-Brittle Transition Temperature
DL Deep Learning
DN Dense Network
DNN Deep Neural Network
DPS Deep Probabilistic Subsampling
DRL Deep Residual Learning
DWT Discrete Wavelet Transform
ECT Eddy Current Testing
EMAT Electro Magnetic Acoustic Transducer
EMD Empirical Mode Decomposition
EWT Empirical Wavelet Transform
FCN Fully Convolutional Neural Network
FE Finite Element
FEM Finite Element Method
FISTA Fast ISTA
FMC Full Matrix Capture
FWHM Full-Width at Half Maximum
FWI Full Waveform Inversion
GAN Generative Adversarial Neural Network
GPCT SNGAN-based generative principal component thermography
GRU Gated Recurrent Unit
HLR Huber Loss Regression
IHCP Inverse Heat Conduction Problem
IIoT Industrial Internet of Things
IR Infrared
IRT Infrared Thermography
ISTA Iterative Shrinkage-Thresholding Algorithm
J-DPS Joint DPS
KPCA Kernel Principal Component Analysis
LCF Low-cycle fatigue
LDA Linear Discriminant Analysis
LISTA Learned ISTA
LSTM Long Short-Term Memory
MAE Mean Absolute Error
ML Machine Learning
MLE Maximum Likelihood Estimator
MLP Multilayer Perceptron
MLR Multiple Linear Regression
MRI Magnetic Resonance Imaging
MSE Mean Squared Error
MT Modulation Thermography
MV Minimum Variance
NDE Nondestructive Evaluation
NDE Nondestructive Evaluation
NN Neural Network
PCA Principle Component Analysis
PCT Principal Component Thermography
PDE Partial Differential Equation
PINN Physics-Informed Neural Network
PoD Probability of Detection
PPT Pulsed Phase Thermography
PSNR Peak Signal-to-Noise Ratio
PT Pulsed Thermography
PW Plane Wave

PWI Plane Wave Imaging
R-CNN Region Based Convolutional Neural Network
RBF Radial Basis Function
RF Random Forest
RMSE Root Mean Squared Error
RNN Recurrent Neural Network
ROI Region of Interest
RPN Region Proposal Network
RPV Reactor Pressure Vessel
SAFT Synthetic Aperture Focusing Technique
SD Standard Deviation
SGD Stochastic Gradient Descent
SIRT Simultaneous Iterative Reconstruction Technique
SNGAN Spectral Normalized GAN
SSD Single Shot MultiBox Detector
STFT Short-Time Fourier Transform
SVD Singular Value Decomposition
SVM Support Vector Machine
SVR Support Vector Regression
TFM Total Focusing Method
TNDE Thermographic NDE
TSR Thermographic Signal Reconstruction
UCT Ultrasound Computed Tomography
UT Ultrasonic Testing
VMD Variational Mode Decomposition
XGBoost extreme Gradient Boosting

References

- [1] S. Cantero-Chinchilla, P. D. Wilcox, and A. J. Croxford. Deep learning in automated ultrasonic NDE—Developments, axioms and opportunities. *NDT & E International*, page 102703, 2022.
- [2] ISO 9712:2021(en) Non-destructive testing - Qualification and certification of NDT personnel, 2021.
- [3] DIN 1324 Teil 2 - Elektromagnetisches Feld - Materialgrößen, May 1988.
- [4] S. Youssef. *Einsatz maschineller Lernalgorithmen zur mikromagnetischen Materialcharakterisierung*. PhD thesis, Universität des Saarlandes, 2021.
- [5] I. Rekanos, T. Theodoulidis, S. Panas, and T. Tsiboukis. Impedance inversion in eddy current testing of layered planar structures via neural networks. *NDT & E International*, 30(2):69–74, April 1997.
- [6] B. Helifa, M. Féliachi, I. Lefkaier, F. Boubenider, A. Zaoui, and N. Lagraa. Characterization of surface cracks using eddy current ndt simulation by 3d-fem and inversion by neural network. *The Applied Computational Electromagnetics Society Journal (ACES)*, pages 187–194, 2016.
- [7] S. Harzallah, R. Rebhi, M. Chabaat, and A. Rabehi. Eddy current modelling using multi-layer perceptron neural networks for detecting surface cracks. *Frattura ed Integrità Strutturale*, 12(45):147–155, June 2018.
- [8] K. Demachi, T. Hori, and S. Perrin. Crack depth estimation of non-magnetic material by convolutional neural network analysis of eddy current testing signal. *Journal of Nuclear Science and Technology*, 57(4):401–407, November 2019.
- [9] A. Bernieri, L. Ferrigno, M. Laracca, and M. Molinara. Crack shape reconstruction in eddy current testing using machine learning systems for regression. *IEEE Transactions on Instrumentation and Measurement*, 57(9):1958–1968, September 2008.
- [10] S.-J. Song and Y.-K. Shin. Eddy current flaw characterization in tubes by neural networks and finite element modeling. *NDT & E International*, 33(4):233–243, June 2000.
- [11] N. Yusa, W. Cheng, Z. Chen, and K. Miya. Generalized neural network approach to eddy current inversion for real cracks. *NDT & E International*, 35(8):609–614, December 2002.
- [12] M. Wrzuszczak and J. Wrzuszczak. Eddy current flaw detection with neural network applications. *Measurement*, 38(2):132–136, September 2005.
- [13] C. Glorieux, J. Moulder, J. Basart, and J. Thoen. The determination of electrical conductivity profiles using neural network inversion of multi-frequency eddy-current data. *Journal of Physics D: Applied Physics*, 32(5):616–622, January 1999.
- [14] B. Rao, B. Raj, T. Jayakumar, and P. Kalyanasundaram. An artificial neural network for eddy current testing of austenitic stainless steel welds. *NDT & E International*, 35(6):393–398, September 2002.
- [15] E. V. Kuzmin, O. E. Gorbunov, P. O. Plotnikov, V. A. Tyukin, and V. A. Bashkin. Application of neural networks for recognizing rail structural elements in magnetic and eddy current defectograms. *Automatic Control and Computer Sciences*, 53(7):628–637, December 2019.
- [16] Q. Cao, D. Liu, Y. He, J. Zhou, and J. Codrington. Nondestructive and quantitative evaluation of wire rope based on radial basis function neural network using eddy current inspection. *NDT & E International*, 46:7–13, March 2012.
- [17] K. B. Ali, A. N. Abdalla, D. Rifai, and M. A. Faraj. Review on system development in eddy current testing and technique for defect classification and characterization. *IET Circuits, Devices & Systems*, 11(4):338–351, March 2017.
- [18] A. N. AbdAlla, M. A. Faraj, F. Samsuri, D. Rifai, K. Ali, and Y. Al-Douri. Challenges in improving the performance of eddy current testing: Review. *Measurement and Control*, 52(1–2):46–64, November 2018.
- [19] M. Maciusowicz and G. Psuj. Classification of grain-oriented electrical steel sheets by magnetic barkhausen noise using time-frequency analysis and selected machine learning algorithms. *Applied Sciences*, 12(23):12469, December 2022.
- [20] P. Wang, L. Zhu, Q. Zhu, X. Ji, H. Wang, G. Tian, and E. Yao. An application of back propagation neural network for the steel stress detection based on barkhausen noise theory. *NDT & E International*, 55:9–14, April 2013.
- [21] Y. Zhang, W. Liu, K. Li, P. Wang, C. Hang, Y. Chen, X. Han, and W. Gao. Application of a back-propagation neural network for mechanical properties prediction of ferromagnetic materials by magnetic barkhausen noise technique. *Insight - Non-Destructive Testing and Condition Monitoring*, 61(2):95–99, February 2019.
- [22] R. Jedamski and J. Epp. Non-destructive micromagnetic determination of hardness and case hardening depth using linear regression analysis and artificial neural networks. *Metals*, 11(1):18, December 2020.
- [23] X. Wang, C. He, P. Li, X. Liu, Z. Xing, and Z. Yan. Micromagnetic and quantitative prediction of surface hardness in carbon steels based on a joint classification-regression method. *Journal of Nondestructive Evaluation*, 41(3), September 2022.
- [24] Z. Xing, X. Wang, M. Ning, C. He, and X. Liu. Micromagnetic and robust evaluation of surface hardness in cr12mov steel considering repeatability of the instrument. *Sensors*, 23(3):1273, January 2023.
- [25] H. Sheng and P. Wang. Evaluation of pipeline steel mechanical property distribution based on multimicromagnetic ndt method. *IEEE Transactions on Instrumentation and Measurement*, 72:1–15, 2023.
- [26] S. Grönroos, J. Rinta-aho, T. Koskinen, and G. Sorger. Combination of non-destructive methods in estimating irradiation-induced reactor pressure vessel steel alloy embrittlement with machine learning. *SSRN Electronic Journal*, 2021.
- [27] S. Youssef, M. Schuppmann, S. Pushkarev, P. Stopp, and O. Stawicki. KI-basierte Prozessoptimierung im Stahlwerk – Multimodales, intelligentes und autoadaptives Sensorsystem zur Hardspotdetektion an Grobblechen. In *ZfP-Zeitung 175*, page 38–44. DGZfP e.V, June 2021.
- [28] C. Zimmer, Y. N. Rallabandi, K. Szielasko, C. Eichheimer, M. Luke, and S. Youssef. Micromagnetic Microstructure- and

- Stress-Independent Materials Characterization in Reactor Safety Research. *Materials*, 14(18), September 2021.
- [29] S. Youssef, C. Zimmer, K. Szielasko, and A. Schütze. Bewertung subjektiver und automatisierter Merkmalsextraktion periodischer Zeitsignale am Beispiel des 3MA-X8-verfahrens. *tm - Technisches Messen*, 86(5):267–277, 2019.
- [30] S. Youssef, C. Zimmer, K. Szielasko, Z. K. Suri, and A. Schütze. Vergleich subjektiver und automatisierter Merkmalsextraktion sowie Einsatz maschineller Lernalgorithmen zur mikromagnetischen Materialcharakterisierung. In *4.3 Machine Learning und Signalverarbeitung*, pages 347–354. 20. GMA/ITG-Fachtagung Sensoren und Messsysteme 2019, June 2019.
- [31] M. D. Verweij, B. E. Treeby, K. W. A. van Dongen, and L. Demi. Simulation of Ultrasound Fields. *Comprehensive Biomedical Physics*, pages 465–499, 2014.
- [32] L. Le Jeune, S. Robert, E. L. Villaverde, and C. Prada. Plane wave imaging for ultrasonic non-destructive testing: Generalization to multimodal imaging. *Ultrasonics*, 64:128–138, 2016.
- [33] M. F. Schiffner. Random incident waves for fast compressed pulse-echo ultrasound imaging, 2019.
- [34] M. F. Schiffner and G. Schmitz. Fast compressive pulse-echo ultrasound imaging using random incident sound fields. *The Journal of the Acoustical Society of America*, 141:3611–3611, 2017.
- [35] O. Çakıroğlu, E. Pérez, F. Roemer, and M. Schiffner. Optimization of transmission parameters in fast pulse-echo ultrasound imaging using sparse recovery. In *2023 31st European Signal Processing Conference (EUSIPCO)*, pages 441–445, 2023.
- [36] O. Çakıroğlu, E. Pérez, F. Roemer, and M. Schiffner. Autoencoder-based Learning of Transmission Parameters in Fast Pulse-Echo Ultrasound Imaging employing Sparse Recovery. In *2023 IEEE International Workshop on Computational Advances in Multi-Sensor Adaptive Processing (CAMSAP)*. IEEE, 2023. In Press.
- [37] I. Daubechies, M. Defrise, and C. De Mol. An iterative thresholding algorithm for linear inverse problems with a sparsity constraint. *Communications on Pure and Applied Mathematics: A Journal Issued by the Courant Institute of Mathematical Sciences*, 57(11):1413–1457, 2004.
- [38] A. Beck and M. Teboulle. A fast iterative shrinkage-thresholding algorithm with application to wavelet-based image deblurring. In *2009 IEEE International Conference on Acoustics, Speech and Signal Processing*, pages 693–696, 2009.
- [39] S. Boyd, N. Parikh, E. Chu, B. Peleato, J. Eckstein, et al. Distributed optimization and statistical learning via the alternating direction method of multipliers. *Foundations and Trends® in Machine Learning*, 3(1):1–122, 2011.
- [40] J. Zhang, Q. He, Y. Xiao, H. Zheng, C. Wang, and J. Luo. Self-supervised learning of a deep neural network for ultrafast ultrasound imaging as an inverse problem. In *2020 IEEE International Ultrasonics Symposium (IUS)*, pages 1–4. IEEE, 2020.
- [41] K. He, X. Zhang, S. Ren, and J. Sun. Deep residual learning for image recognition. In *Proceedings of the IEEE conference on computer vision and pattern recognition*, pages 770–778, 2016.
- [42] H. Yao, F. Dai, S. Zhang, Y. Zhang, Q. Tian, and C. Xu. Dr2-net: Deep residual reconstruction network for image compressive sensing. *Neurocomputing*, 359:483–493, 2019.
- [43] K. Kulkarni, S. Lohit, P. Turaga, R. Kerviche, and A. Ashok. Reconnet: Non-iterative reconstruction of images from compressively sensed measurements. In *2016 IEEE Conference on Computer Vision and Pattern Recognition (CVPR)*, pages 449–458, 2016.
- [44] M. Mardani, E. Gong, J. Y. Cheng, S. S. Vasanawala, G. Zaharchuk, L. Xing, and J. M. Pauly. Deep generative adversarial neural networks for compressive sensing mri. *IEEE Transactions on Medical Imaging*, 38(1):167–179, 2019.
- [45] B. W. Drinkwater and P. D. Wilcox. Ultrasonic arrays for non-destructive evaluation: A review. *NDT & e International*, 39(7):525–541, 2006.
- [46] J.-H. Kim, A. Basarab, P. R. Hill, D. R. Bull, D. Kouamé, and A. Achim. Ultrasound image reconstruction from compressed measurements using approximate message passing. In *2016 24th European Signal Processing Conference (EUSIPCO)*, pages 557–561. IEEE, 2016.
- [47] S. Liu, Y. Wang, X. Yang, B. Lei, L. Liu, S. X. Li, D. Ni, and T. Wang. Deep learning in medical ultrasound analysis: a review. *Engineering*, 5(2):261–275, 2019.
- [48] R. J. Van Sloun, R. Cohen, and Y. C. Eldar. Deep learning in ultrasound imaging. *Proceedings of the IEEE*, 108(1):11–29, 2019.
- [49] N. Shlezinger, Y. C. Eldar, and S. P. Boyd. Model-based deep learning: On the intersection of deep learning and optimization. *IEEE Access*, 10:115384–115398, 2022.
- [50] K. Gregor and Y. LeCun. Learning fast approximations of sparse coding. In *Proceedings of the 27th international conference on international conference on machine learning*, pages 399–406, 2010.
- [51] V. Monga, Y. Li, and Y. C. Eldar. Algorithm unrolling: Interpretable, efficient deep learning for signal and image processing. *IEEE Signal Processing Magazine*, 38(2):18–44, 2021.
- [52] A. Bora, A. Jalal, E. Price, and A. G. Dimakis. Compressed sensing using generative models. In *International conference on machine learning*, pages 537–546. PMLR, 2017.
- [53] R. J. van Sloun, J. C. Ye, and Y. C. Eldar. Deep learning for ultrasound beamforming. *arXiv preprint arXiv:2109.11431*, 2021.
- [54] B. Luijten, N. Chennakeshava, Y. C. Eldar, M. Mischi, and R. J. van Sloun. Ultrasound signal processing: from models to deep learning. *Ultrasound in Medicine & Biology*, 2023.
- [55] B. Luijten, R. Cohen, F. J. De Bruijn, H. A. Schmeitz, M. Mischi, Y. C. Eldar, and R. J. Van Sloun. Deep learning for fast adaptive beamforming. In *ICASSP 2019-2019 IEEE International Conference on Acoustics, Speech and Signal Processing (ICASSP)*, pages 1333–1337. IEEE, 2019.
- [56] B. Luijten, R. Cohen, F. J. De Bruijn, H. A. Schmeitz, M. Mischi, Y. C. Eldar, and R. J. Van Sloun. Adaptive ultrasound beamforming using deep learning. *IEEE Transactions on Medical Imaging*, 39(12):3967–3978, 2020.
- [57] Y. Li, O. Bar-Shira, V. Monga, and Y. C. Eldar. Deep algorithm unrolling for biomedical imaging. *arXiv preprint arXiv:2108.06637*, 2021.
- [58] C. Khan, R. J. van Sloun, and B. Byram. Unfolding model-based beamforming for high quality ultrasound imaging. In *ICASSP 2022-2022 IEEE International Conference on Acoustics, Speech and Signal Processing (ICASSP)*, pages 8682–8686. IEEE, 2022.
- [59] O. Solomon, R. Cohen, Y. Zhang, Y. Yang, Q. He, J. Luo, R. J. van Sloun, and Y. C. Eldar. Deep unfolded robust pca with application to clutter suppression in ultrasound. *IEEE transactions on medical imaging*, 39(4):1051–1063, 2019.
- [60] T. Chernyakova and Y. C. Eldar. Fourier-domain beamforming: the path to compressed ultrasound imaging. *IEEE transactions on ultrasonics, ferroelectrics, and frequency control*, 61(8):1252–1267, 2014.
- [61] R. Cohen and Y. C. Eldar. Sparse convolutional beamforming for ultrasound imaging. *IEEE transactions on ultrasonics, ferroelectrics, and frequency control*, 65(12):2390–2406, 2018.
- [62] A. Mamistvalov and Y. C. Eldar. Deep unfolded recovery of sub-nyquist sampled ultrasound images. *IEEE Transactions on Ultrasonics, Ferroelectrics, and Frequency Control*, 68(12):3484–3496, 2021.
- [63] I. A. Huijben, B. S. Veeling, K. Janse, M. Mischi, and R. J. van Sloun. Learning sub-sampling and signal recovery with applications in ultrasound imaging. *IEEE Transactions on Medical Imaging*, 39(12):3955–3966, 2020.
- [64] E. Pérez, J. Kirchoff, F. Krieg, and F. Römer. Subsampling approaches for compressed sensing with ultrasound arrays in non-destructive testing. *Sensors*, 20(23):6734, 2020.
- [65] H. Wang, E. Pérez, and F. Römer. Deep Learning-Assisted optimal sensor placement in ultrasound NDT. In *Proceedings of the AMA Sensor and Measurement Science International (SMSI) Conference 2023*, Nuremberg, Germany, May 2023.

- [66] H. Wang, E. Pérez, and F. Römer. Deep learning-based optimal spatial subsampling in ultrasound nondestructive testing. In *2023 31st European Signal Processing Conference (EUSIPCO)*, pages 1863–1867, 2023.
- [67] H. Wang, E. Pérez, and F. Römer. Data-Driven subsampling matrices design for phased array ultrasound nondestructive testing. In *Proceedings of the 2023 IEEE International Ultrasonics Symposium (IUS-2023)*, Montreal, Canada, September 2023.
- [68] H. Wang, Y. Zhou, E. Pérez, and F. Römer. Jointly learning selection matrices for transmitters, receivers and fourier coefficients in multichannel imaging. In *Proceedings of the 2024 IEEE International Conference on Acoustics, Speech and Signal Processing (ICASSP-2024)*, Seoul, Korea, April 2024.
- [69] M. T. M. Khairi, S. Ibrahim, M. A. M. Yunus, M. Faramarzi, G. P. Sean, J. Puspanathan, and A. Abid. Ultrasound computed tomography for material inspection: Principles, design and applications. *Measurement*, 146:490–523, 2019.
- [70] J. Gubernatis, E. Domany, J. Krumhansl, and M. Huberman. The Born approximation in the theory of the scattering of elastic waves by flaws. *Journal of Applied Physics*, 48(7):2812–2819, 1977.
- [71] M. Zielińska and M. Rucka. Non-Destructive Assessment of Masonry Pillars using Ultrasonic Tomography. *Materials*, 11(12):2543, 2018.
- [72] V. G. Haach and F. C. Ramirez. Qualitative assessment of concrete by ultrasound tomography. *Construction and Building Materials*, 119:61–70, 2016.
- [73] N. Duric, P. Littrup, L. Poulo, A. Babkin, R. Pevzner, E. Holsapple, O. Rama, and C. Glide. Detection of breast cancer with ultrasound tomography: First results with the Computed Ultrasound Risk Evaluation (CURE) prototype. *Medical physics*, 34(2):773–785, 2007.
- [74] J. Virieux, A. Asnaashari, R. Brossier, L. Métivier, A. Ribodetti, and W. Zhou. An introduction to full waveform inversion. In *Encyclopedia of exploration geophysics*, pages R1–1. Society of Exploration Geophysicists, 2017.
- [75] L. Guasch, O. Calderón Agudo, M.-X. Tang, P. Nachev, and M. Warner. Full-waveform inversion imaging of the human brain. *NPIJ digital medicine*, 3(1):28, 2020.
- [76] G. Kłosowski, T. Rymarczyk, K. Kania, A. Świć, and T. Cieplak. Maintenance of industrial reactors supported by deep learning driven ultrasound tomography. *Eksploracja i Niezawodność*, 22(1):138–147, 2020.
- [77] T. Lähivaara, L. Kärkkäinen, J. M. J. Huttunen, and J. S. Hesthaven. Deep convolutional neural networks for estimating porous material parameters with ultrasound tomography. *The Journal of the Acoustical Society of America*, 143(2):1148–1158, 2018.
- [78] X. Long, J. Chen, W. Liu, and C. Tian. Deep Learning Ultrasound Computed Tomography under Sparse Sampling. *IEEE Transactions on Ultrasonics, Ferroelectrics, and Frequency Control*, 2023.
- [79] O. Ronneberger, P. Fischer, and T. Brox. U-Net: Convolutional Networks for Biomedical Image Segmentation. In *Medical Image Computing and Computer-Assisted Intervention—MICCAI 2015: 18th International Conference, Munich, Germany, October 5–9, 2015, Proceedings, Part III 18*, pages 234–241. Springer, 2015.
- [80] M. Feigin, D. Freedman, and B. W. Anthony. A Deep Learning Framework for Single-Sided Sound Speed Inversion in Medical Ultrasound. *IEEE Transactions on Biomedical Engineering*, 67(4):1142–1151, 2019.
- [81] M. Raissi, P. Perdikaris, and G. E. Karniadakis. Physics-Informed Neural Networks: A Deep Learning Framework for Solving Forward and Inverse Problems Involving Nonlinear Partial Differential Equations. *Journal of Computational Physics*, 378:686–707, 2019.
- [82] B. Moseley, A. Markham, and T. Nissen-Meyer. Solving the wave equation with physics-informed deep learning. *arXiv preprint arXiv:2006.11894*, 2020.
- [83] M. Rasht-Behesht, C. Huber, K. Shukla, and G. E. Karniadakis. Physics-Informed Neural Networks (PINNs) for Wave Propagation and Full Waveform Inversions. *Journal of Geophysical Research: Solid Earth*, 127(5):e2021JB023120, 2022.
- [84] K. Shukla, P. C. Di Leoni, J. Blackshire, D. Sparkman, and G. E. Karniadakis. Physics-Informed Neural Network for Ultrasound Nondestructive Quantification of Surface Breaking Cracks. *Journal of Nondestructive Evaluation*, 39:1–20, 2020.
- [85] H. Sun, P. Ramuhalli, and R. E. Jacob. Machine learning for ultrasonic nondestructive examination of welding defects: A systematic review. *Ultrasonics*, 127:106854, 2023.
- [86] I. Daubechies. The wavelet transform, time-frequency localization and signal analysis. *IEEE Transactions on Information Theory*, 36(5):961–1005, 1990.
- [87] D.-Z. Dang, C.-C. Lai, Y.-Q. Ni, Q. Zhao, B. Su, and Q.-F. Zhou. Image classification-based defect detection of railway tracks using fiber bragg grating ultrasonic sensors. *Applied Sciences*, 13(1), 2023.
- [88] Y. Jiang, H. Wang, G. Tian, Q. Yi, J. Zhao, and K. Zhen. Fast classification for rail defect depths using a hybrid intelligent method. *Optik*, 180:455–468, 2019.
- [89] G. Lv, S. Guo, D. Chen, H. Feng, K. Zhang, Y. Liu, and W. Feng. Laser ultrasonics and machine learning for automatic defect detection in metallic components. *NDT & E International*, 133:102752, 2023.
- [90] Y. Freund and R. E. Schapire. A decision-theoretic generalization of on-line learning and an application to boosting. In P. Vitányi, editor, *Computational Learning Theory*, pages 23–37. Berlin, Heidelberg, 1995. Springer Berlin Heidelberg.
- [91] T. Chen, T. He, M. Benesty, V. Khotilovich, Y. Tang, H. Cho, K. Chen, R. Mitchell, I. Cano, T. Zhou, et al. Xgboost: extreme gradient boosting. *R package version 0.4-2*, 1(4):1–4, 2015.
- [92] M. Hearst, S. Dumais, E. Osuna, J. Platt, and B. Scholkopf. Support vector machines. *IEEE Intelligent Systems and their Applications*, 13(4):18–28, 1998.
- [93] Y. Yan, D. Liu, B. Gao, G. Y. Tian, and Z. C. Cai. A deep learning-based ultrasonic pattern recognition method for inspecting girth weld cracking of gas pipeline. *IEEE Sensors Journal*, 20(14):7997–8006, 2020.
- [94] Y. Chen, S. Liang, Z. Wang, H. Ma, M. Dong, D. Liu, and X. Wan. Automatic classification of weld defects from ultrasonic signals using wpee-kpca feature extraction and an abc-svm approach. *Insight - Non-Destructive Testing and Condition Monitoring*, 65(5):262–269, 2023.
- [95] P. Pawar and R. Buktar. Detection and classification of defects in ultrasonic testing using deep learning. In V. K. Gunjan and J. M. Zurada, editors, *Proceedings of the 2nd International Conference on Recent Trends in Machine Learning, IoT, Smart Cities and Applications*, pages 1–15. Singapore, 2022. Springer Nature Singapore.
- [96] A. Arbaoui, A. Ouahabi, S. Jacques, and M. Hamiane. Concrete cracks detection and monitoring using deep learning-based multiresolution analysis. *Electronics*, 10(15), 2021.
- [97] A. Arbaoui, A. Ouahabi, S. Jacques, and M. Hamiane. Wavelet-based multiresolution analysis coupled with deep learning to efficiently monitor cracks in concrete. *Frattura ed Integrità Strutturale / Fracture and Structural Integrity*, 15(58):33–47, 2021.
- [98] K. Sudheera, N. M. Nandhitha, V. B. Venkat Sai, and N. V. Kumar. Deep learning techniques for flaw characterization in weld pieces from ultrasonic signals. *Russian Journal of Nondestructive Testing*, 56:820–830, 2020.
- [99] S. Hochreiter and J. Schmidhuber. Long short-term memory. *Neural computation*, 9(8):1735–1780, 1997.
- [100] K. Virupakshappa and E. Oruklu. Unsupervised machine learning for ultrasonic flaw detection using gaussian mixture modeling, k-means clustering and mean shift clustering. In *2019 IEEE International Ultrasonics Symposium (IUS)*, pages 647–649, 2019.
- [101] M. A. Oliveira, E. F. Simas Filho, M. C. Albuquerque, Y. T. Santos, I. C. da Silva, and C. T. Farias. Ultrasound-based identification of damage in wind turbine blades using novelty detection. *Ultrasonics*, 108:106166, 2020.
- [102] J. Gilles. Empirical wavelet transform. *IEEE Transactions on Signal Processing*, 61(16):3999–4010, 2013.

- [103] N. E. Huang, Z. Shen, S. R. Long, M. C. Wu, H. H. Shih, Q. Zheng, N.-C. Yen, C. C. Tung, and H. H. Liu. The empirical mode decomposition and the hilbert spectrum for nonlinear and non-stationary time series analysis. *Proceedings of the Royal Society of London. Series A: mathematical, physical and engineering sciences*, 454(1971):903–995, 1998.
- [104] M. Zhang, Q. Zhang, J. Li, J. Xu, and J. Zheng. Classification of acoustic emission signals in wood damage and fracture process based on empirical mode decomposition, discrete wavelet transform methods, and selected features. *Journal of Wood Science*, 67(1):1–13, 2021.
- [105] K. Dragomiretskiy and D. Zosso. Variational mode decomposition. *IEEE Transactions on Signal Processing*, 62(3):531–544, 2014.
- [106] M. Mousavi and A. H. Gandomi. Wood hole-damage detection and classification via contact ultrasonic testing. *Construction and Building Materials*, 307:124999, 2021.
- [107] H. Sun, L. Peng, S. Wang, S. Huang, and K. Qu. Development of frequency-mixed point-focusing shear horizontal guided-wave emat for defect inspection using deep neural network. *IEEE Transactions on Instrumentation and Measurement*, 70:1–14, 2021.
- [108] S. Lohit, K. Kulkarni, and P. Turaga. Direct inference on compressive measurements using convolutional neural networks. In *2016 IEEE international conference on image processing (ICIP)*, pages 1913–1917. IEEE, 2016.
- [109] Y. Lecun, L. Bottou, Y. Bengio, and P. Haffner. Gradient-based learning applied to document recognition. *Proceedings of the IEEE*, 86(11):2278–2324, 1998.
- [110] Y. Jia, E. Shelhamer, J. Donahue, S. Karayev, J. Long, R. Girshick, S. Guadarrama, and T. Darrell. Caffe: Convolutional architecture for fast feature embedding. In *Proceedings of the 22nd ACM international conference on Multimedia*, pages 675–678, 2014.
- [111] M. A. Davenport, M. F. Duarte, M. B. Wakin, J. N. Laska, D. Takhar, K. F. Kelly, and R. G. Baraniuk. The smashed filter for compressive classification and target recognition. In *Computational Imaging V*, volume 6498, pages 142–153. SPIE, 2007.
- [112] Y. Guo, Z. Xiao, L. Geng, J. Wu, F. Zhang, Y. Liu, and W. Wang. Fully convolutional neural network with gru for 3d braided composite material flaw detection. *IEEE Access*, 7:151180–151188, 2019.
- [113] J. M. Ha, H. M. Seung, and W. Choi. Autoencoder-based detection of near-surface defects in ultrasonic testing. *Ultrasonics*, 119:106637, 2022.
- [114] R. Calderbank, S. Jafarpour, and R. Schapir. Compressed learning : Universal sparse dimensionality reduction and learning in the measurement domain. *preprint*, 2009.
- [115] S. Cantero-Chinchilla, P. D. Wilcox, and A. J. Croxford. Deep learning in automated ultrasonic nde – developments, axioms and opportunities. *NDT & E International*, 131:102703, 2022.
- [116] M. Aharon, M. Elad, and A. Bruckstein. K-svd: An algorithm for designing overcomplete dictionaries for sparse representation. *IEEE Transactions on Signal Processing*, 54(11):4311–4322, 2006.
- [117] Y. Song, C. Ge, N. Song, and M. Deng. A novel dictionary learning-based approach for ultrasound elastography denoising. *Mathematical Biosciences and Engineering*, 19(11):11533–11543, 2022.
- [118] I. Tošić, I. Jovanovic, P. Frossard, M. Vetterli, and N. Duric. Ultrasound tomography image reconstruction with learned dictionaries. In *Proceedings of the IEEE International Conference on Acoustics, Speech, and Signal Processing (ICASSP 2010)*, pages 5502–5505, Dallas, TX, USA, March 2010.
- [119] B. A. Olshausen and D. J. Field. Emergence of simple-cell receptive field properties by learning a sparse code for natural images. *Nature*, 381(6583):607–609, 1996.
- [120] I. Virkkunen, T. Koskinen, and O. Siljama. Virtual round robin 2-Phased array inspection of dissimilar metal welds. *Nuclear Engineering and Design*, 414:112555, 2023.
- [121] R. J. Pyle, R. R. Hughes, A. A. S. Ali, and P. D. Wilcox. Uncertainty quantification for deep learning in ultrasonic crack characterization. *IEEE Transactions on Ultrasonics, Ferroelectrics, and Frequency Control*, 69(7):2339–2351, Jul 2022.
- [122] T. Gantala and K. Balasubramaniam. Automated defect recognition for welds using simulation assisted tfm imaging with artificial intelligence. *Journal of Nondestructive Evaluation*, 40(1), Feb 2021.
- [123] A. Bochkovskiy, C.-Y. Wang, and H.-Y. M. Liao. YOLOv4: Optimal Speed and Accuracy of Object Detection. *arXiv preprint arXiv:2004.10934*, 2020.
- [124] L. Posilović, D. Medak, M. Subašić, M. Budimir, and S. Lončarić. Generating ultrasonic images indistinguishable from real images using generative adversarial networks. *Ultrasonics*, 119:106610, Feb 2022.
- [125] P. Isola, J.-Y. Zhu, T. Zhou, and A. A. Efros. Image-to-Image Translation with Conditional Adversarial Networks. In *Proceedings of the IEEE Conference on Computer Vision and Pattern Recognition*, pages 1125–1134, 2017.
- [126] J. Redmon and A. Farhadi. YOLOv3: An Incremental Improvement. *arXiv preprint arXiv:1804.02767*, 2018.
- [127] T. Park, M.-Y. Liu, T.-C. Wang, and J.-Y. Zhu. Semantic Image Synthesis with Spatially-Adaptive Normalization. In *Proceedings of the IEEE/CVF conference on computer vision and pattern recognition*, pages 2337–2346, 2019.
- [128] T.-C. Wang, M.-Y. Liu, J.-Y. Zhu, A. Tao, J. Kautz, and B. Catanzaro. High-Resolution Image Synthesis and Semantic Manipulation with Conditional GANs. In *Proceedings of the IEEE conference on computer vision and pattern recognition*, pages 8798–8807, 2018.
- [129] J. Singh, K. Tant, A. Curtis, and A. Mulholland. Real-time super-resolution mapping of locally anisotropic grain orientations for ultrasonic non-destructive evaluation of crystalline material. *Neural Computing and Applications*, 34(6):4993–5010, Nov 2021.
- [130] B. Ni and H. Gao. A deep learning approach to the inverse problem of modulus identification in elasticity. *MRS Bulletin*, 46(1):19–25, Jan 2021.
- [131] M. Mirza and S. Osindero. Conditional generative adversarial nets. *arXiv preprint arXiv:1411.1784*, 2014.
- [132] C. Song, T. Alkhalifah, and U. B. Waheed. A versatile framework to solve the helmholtz equation using physics-informed neural networks. *Geophysical Journal International*, 228(3):1750–1762, 10 2021.
- [133] C. Offen and S. Ober-Blöbaum. Learning discrete lagrangians for variational PDEs from data and detection of travelling waves. In *Lecture Notes in Computer Science*, pages 569–579. Springer Nature Switzerland, 2023.
- [134] G. E. Karniadakis, I. G. Kevrekidis, L. Lu, P. Perdikaris, S. Wang, and L. Yang. Physics-informed machine learning. *Nature Review Physics*, 3:422–440, 2021.
- [135] D. P. Almond and S. Lau. Defect sizing by transient thermography. i. an analytical treatment. *Journal of Physics D: Applied Physics*, 27(5):1063, 1994.
- [136] X. Maldague and S. Marinetti. Pulse phase infrared thermography. *Journal of applied physics*, 79(5):2694–2698, 1996.
- [137] U. Netzelmann and D. Müller. Modified pulse-phase thermography algorithms for improved contrast-to-noise ratio from pulse-excited thermographic sequences. *NDT & E International*, 116:102325, 2020.
- [138] G. Poelman, S. Hedayatrasa, J. Segers, W. Van Paepegem, and M. Kersemans. Adaptive spectral band integration in flash thermography: Enhanced defect detectability and quantification in composites. *Composites Part B: Engineering*, 202:108305, 2020.
- [139] N. Rajic. Principal component thermography for flaw contrast enhancement and flaw depth characterisation in composite structures. *Composite Structures*, 58(4):521–528, 2002.
- [140] B. Milovanović, M. Gaši, and S. Gumbarević. Principal component thermography for defect detection in concrete. *Sensors*, 20(14):3891, 2020.
- [141] M. Omar, R. Parvataneni, and Y. Zhou. A combined approach of self-referencing and principle component thermography for transient, steady, and selective heating scenarios. *Infrared physics & technology*, 53(5):358–362, 2010.
- [142] Y. Liu, F. Wang, Z. Jiang, S. Sfarra, K. Liu, and Y. Yao. Generative deep learning-based thermographic inspection of artwork. *Sensors*, 23(14):6362, 2023.

- [143] H. Zhong, S. Yu, H. Trinh, Y. Lv, R. Yuan, and Y. Wang. Fine-tuning transfer learning based on dcgan integrated with self-attention and spectral normalization for bearing fault diagnosis. *Measurement*, 210:112421, 2023.
- [144] S. M. Shepard. Advances in thermographic ndt. In *Infrared Technology and Applications XXIX*, volume 5074, pages 882–887. SPIE, 2003.
- [145] J. Roche, F. Leroy, and D. Balageas. Images of thermographic signal reconstruction coefficients: A simple way for rapid and efficient detection of discontinuities. *Materials evaluation*, 72(1):73–82, 2014.
- [146] A. Schager, G. Zauner, G. Mayr, and P. Burgholzer. Extension of the thermographic signal reconstruction technique for an automated segmentation and depth estimation of subsurface defects. *Journal of Imaging*, 6(9):96, 2020.
- [147] Q. Feng, B. Gao, P. Lu, W. L. Woo, Y. Yang, Y. Fan, X. Qiu, and L. Gu. Automatic seeded region growing for thermography debonding detection of cfrp. *Ndt & E International*, 99:36–49, 2018.
- [148] A. Ratsakou, A. Skarlatos, C. Reboud, and D. Lesselier. Shape reconstruction of delamination defects using thermographic infrared signals based on an enhanced canny approach. *Infrared Physics & Technology*, 111:103527, 2020.
- [149] M.-M. Groz, E. Abisset-Chavanne, A. Meziane, A. Sommier, and C. Pradère. Three-dimensional reconstruction of thermal volumetric sources from surface temperature fields measured by infrared thermography. *Applied Sciences*, 9(24):5464, 2019.
- [150] P. Burgholzer, M. Thor, J. Gruber, and G. Mayr. Three-dimensional thermographic imaging using a virtual wave concept. *Journal of Applied Physics*, 121(10), 2017.
- [151] P. Kovács, B. Lehner, G. Thummerer, G. Mayr, P. Burgholzer, and M. Huemer. Deep learning approaches for thermographic imaging. *Journal of Applied Physics*, 128, 10 2020.
- [152] D. Gillsjö, G. Flood, and K. Åström. Semantic room wireframe detection from a single view. In *2022 26th International Conference on Pattern Recognition (ICPR)*, pages 1886–1893. IEEE, 2022.
- [153] Y. Zhou, A. Osman, M. Willms, A. Kunz, S. Philipp, J. Blatt, and S. Eul. Semantic wireframe detection. In *DGZfP Jahrestagung 2023*, Friedrichshafen, 2023.
- [154] S. Guan, N. Kamona, and M. Loew. Segmentation of thermal breast images using convolutional and deconvolutional neural networks. In *2018 IEEE Applied Imagery Pattern Recognition Workshop (AIPR)*, Washington DC, USA, 10 2018.
- [155] O. Pedrayes, D. Lema, R. Usamentiaga, V. Pablo, and F. D. Garcia. Semantic segmentation for non-destructive testing with step-heating thermography for composite laminates. *Measurement*, 200:111653, 07 2022.
- [156] D. Müller, U. Netzelmann, and B. Valeske. Defect shape detection and defect reconstruction in active thermography by means of two-dimensional convolutional neural network as well as spatiotemporal convolutional lstm network. *Quantitative InfraRed Thermography Journal*, 19:1–19, 09 2020.
- [157] A. A. R. M. A. Ebayyeh and A. Mousavi. A review and analysis of automatic optical inspection and quality monitoring methods in electronics industry. *IEEE Access*, 8:183192–183271, 2020.
- [158] C. Demant, B. Streicher-Abel, and A. Springhoff. *Industrielle Bildverarbeitung: Wie optische Qualitätskontrolle wirklich funktioniert*. Springer Berlin Heidelberg, 2011.
- [159] P. Bharati and A. Pramanik. Deep learning techniques—r-cnn to mask r-cnn: a survey. *Computational Intelligence in Pattern Recognition: Proceedings of CIPR 2019*, pages 657–668, 2020.
- [160] S. Ren, K. He, R. Girshick, and J. Sun. Faster r-cnn: Towards real-time object detection with region proposal networks, 2016.
- [161] K. Simonyan and A. Zisserman. Very deep convolutional networks for large-scale image recognition, 2015.
- [162] M. Everingham, S. M. A. Eslami, L. Van Gool, C. K. I. Williams, J. Winn, and A. Zisserman. The pascal visual object classes challenge: A retrospective. *International Journal of Computer Vision*, 111(1):98–136, January 2015.
- [163] T.-Y. Lin, M. Maire, S. Belongie, L. Bourdev, R. Girshick, J. Hays, P. Perona, D. Ramanan, C. L. Zitnick, and P. Dollár. Microsoft coco: Common objects in context, 2015.
- [164] W. Liu, D. Anguelov, D. Erhan, C. Szegedy, S. Reed, C.-Y. Fu, and A. C. Berg. Ssd: Single shot multibox detector. In *Computer Vision—ECCV 2016: 14th European Conference, Amsterdam, The Netherlands, October 11–14, 2016, Proceedings, Part I 14*, pages 21–37. Springer, 2016.
- [165] P. Jiang, D. Ergu, F. Liu, Y. Cai, and B. Ma. A review of yolo algorithm developments. *Procedia Computer Science*, 199:1066–1073, 2022.
- [166] J. Redmon, S. Divvala, R. Girshick, and A. Farhadi. You only look once: Unified, real-time object detection, 2016.
- [167] G. Jocher, A. Chaurasia, and J. Qiu. Yolo by ultralytics. <https://github.com/ultralytics/>, 2023. Accessed on 12 January 2023.
- [168] K. He, G. Gkioxari, P. Dollár, and R. Girshick. Mask r-cnn, 2018.
- [169] E. Shelhamer, J. Long, and T. Darrell. Fully convolutional networks for semantic segmentation. *IEEE Transactions on Pattern Analysis and Machine Intelligence*, 39(4):640–651, 2017.
- [170] I. Katsamenis, E. Protopapadakis, A. Doulamis, N. Doulamis, and A. Voulodimos. Pixel-level corrosion detection on metal constructions by fusion of deep learning semantic and contour segmentation, 2020.
- [171] C. Szegedy, V. Vanhoucke, S. Ioffe, J. Shlens, and Z. Wojna. Rethinking the inception architecture for computer vision, 2015.
- [172] C. Wang, F. Shi, M. Zhao, J. Ao, C. Jia, and S. Chen. Convolutional Neural Network-Based Terahertz Spectral Classification of Liquid Contraband for Security Inspection. *IEEE Sensors Journal*, 21(17):18955–18963, 2021.
- [173] Z. Xiao, K.-Y. Song, and M. M. Gupta. Development of a CNN edge detection model of noised X-ray images for enhanced performance of non-destructive testing. *Measurement*, 174:109012, 2021.
- [174] S. S. A. Zaidi, M. S. Ansari, A. Aslam, N. Kanwal, M. Asghar, and B. Lee. A survey of modern deep learning based object detection models. *Digital Signal Processing*, 126:103514, 2022.
- [175] T. Van De Looverbosch, B. Vandenbussche, P. Verboven, and B. Nicolai. Nondestructive high-throughput sugar beet fruit analysis using X-ray CT and deep learning. *Computers and Electronics in Agriculture*, 200:107228, 2022.
- [176] B. Hena, Z. Wei, C. I. Castanedo, and X. Maldague. Deep Learning Neural Network Performance on NDT Digital X-ray Radiography Images: Analyzing the Impact of Image Quality Parameters—An Experimental Study. *Sensors*, 23(9):4324, 2023.
- [177] Y. Jiang, G. Li, H. Ge, F. Wang, L. Li, X. Chen, M. Lu, and Y. Zhang. Machine Learning and Application in Terahertz Technology: A Review on Achievements and Future Challenges. *IEEE Access*, 10:53761–53776, 2022.
- [178] S. Helal, H. Sareddeen, H. Dahrouj, T. Y. Al-Naffouri, and M.-S. Alouini. Signal Processing and Machine Learning Techniques for Terahertz Sensing: An overview. *IEEE Signal Processing Magazine*, 39(5):42–62, 2022.
- [179] A. Mamistvalov, A. Amar, N. Kessler, and Y. C. Eldar. Deep-learning based adaptive ultrasound imaging from sub-nyquist channel data. *IEEE Transactions on Ultrasonics, Ferroelectrics, and Frequency Control*, 69(5):1638–1648, 2022.
- [180] D. Perdios, M. Vonlanthen, F. Martinez, M. Arditi, and J.-P. Thiran. Cnn-based image reconstruction method for ultrafast ultrasound imaging. *IEEE Transactions on Ultrasonics, Ferroelectrics, and Frequency Control*, 69(4):1154–1168, 2021.
- [181] C. J. Schuler, M. Hirsch, S. Harmeling, and B. Schölkopf. Learning to Deblur. *IEEE Transactions on Pattern Analysis and Machine Intelligence*, 38(7):1439–1451, 2016.
- [182] D. L. Balageas, J.-M. Roche, F.-H. Leroy, W.-M. Liu, and A. M. Gorbach. The thermographic signal reconstruction method: A powerful tool for the enhancement of transient thermographic images. *Biocybernetics and biomedical engineering*, 35(1):1–9, 2015.
- [183] G. Batchuluun, Y. Lee, D. Nguyen, T. Pham, and K. Park. Thermal image reconstruction using deep learning. *IEEE Access*, PP:1–1, 07

2020.

- [184] P. Sahoo, S. Soltani, and A. Wong. A survey of thresholding techniques. *Computer Vision, Graphics, and Image Processing*, 41(2):233–260, 1988.